

A Comprehensive Interpretation of Fermi-LAT Pulsars: Fundamental-Plane Death Border, Visibility Thresholds, and GeV-TeV Unification

CONSTANTINOS KALAPOTHARAKOS ,¹ ZORAWAR WADIASINGH ,^{2,1,3} ALICE K. HARDING ,⁴ DEMOSTHENES KAZANAS ,¹
 AND DIMITRIOS SKIATHAS ,^{5,1,3,6}

¹ *Astrophysics Science Division, NASA Goddard Space Flight Center, Greenbelt, MD 20771, USA*

² *Department of Astronomy, University of Maryland, College Park, College Park, MD 20742, USA*

³ *Center for Research and Exploration in Space Science and Technology, NASA GSFC, Greenbelt, MD 20771, USA*

⁴ *Theoretical Division, Los Alamos National Laboratory, Los Alamos, NM 87545, USA*

⁵ *Southeastern Universities Research Association, Washington, DC 20005, USA*

⁶ *Department of Physics, University of Patras, Rio, 26504, Greece*

ABSTRACT

We present a framework that links equatorial-current-sheet (ECS) physics to catalog-level phase-averaged gamma-ray pulsar properties. Guided by analytic scalings and 3D particle-in-cell (PIC) simulations, we show that the pulsar “Fundamental Plane” (relating gamma-ray luminosity, spectral cutoff energy, spin-down power $\dot{\mathcal{E}}$, and surface magnetic field) is bounded by two regimes: a radiation-reaction-limited branch and a potential-drop-limited branch. Their intersection defines a transition in $\dot{\mathcal{E}}$ that maps to a gamma-ray visibility threshold on the $P - \dot{P}$ diagram, above which detectability is set by distance and beaming, and below which both cutoff energy and efficiency decline rapidly. Placing ATNF pulsars and McGill magnetars onto these planes reproduces the observed Fermi occupancy, with millisecond pulsars (MSPs) on the observable side, young pulsars (YPs) straddling the threshold, and magnetars clustering at or just below it. At higher $\dot{\mathcal{E}}$, both MSPs and YPs depart from the maximal radiation-reaction-limited envelope at similar cutoff energies, suggesting that enhanced pair creation screens the accelerating electric field in the ECS. We interpret this behavior with a compactness-based criterion for optically thin $\gamma\gamma$ pair feedback in or near the ECS and briefly note an extension to $\gamma\gamma \rightarrow \mu^\pm$ that could yield pulsed multi-TeV neutrinos in the most energetic systems. The framework predicts an MeV-bright, GeV-faint corridor below current Fermi sensitivity, a target for next-generation MeV missions. Finally, motivated by the recent H.E.S.S. II detection of pulsed multi-TeV emission from Vela, we use PIC particle distributions with a simple seed-photon model to reproduce a multi-TeV inverse-Compton component alongside the GeV curvature emission, supporting a unified ECS-based GeV-TeV origin.

Keywords: pulsars: general — stars: neutron — gamma rays: stars — radiation mechanisms: non-thermal — magnetars

1. INTRODUCTION

The Fermi Large Area Telescope (LAT) has revolutionized our understanding of pulsars as powerful gamma-ray emitters. Since its launch, LAT has uncovered a rich and diverse population of gamma-ray pulsars, including young, energetic pulsars (YPs), and older recycled pulsars (the millisecond pulsars, MSPs), including radio-quiet pulsars. Through precise measurements of their spectra and pulse profiles, LAT has firmly established gamma-ray emission as a common characteristic of rotation-powered pulsars. The energetic output of these pulsars peaks in the LAT band (photon energies of order GeV), providing the most direct constraints on the structure of their magnetospheres, the locations of particle acceleration, and emission models. Collectively, LAT pulsars serve as a powerful probe of magnetospheric physics across a wide range of evolutionary stages and physical parameters.

In parallel with these observational breakthroughs, substantial theoretical progress has transformed our understanding of pulsar magnetospheres. A foundational step was the development of global solutions under the force-free (FF) approximation, where the plasma is sufficiently dense to enforce the ideal conditions $\vec{E} \cdot \vec{B} = 0$ and $E < B$ throughout the magnetosphere for local electric and magnetic fields E and B . These FF models revealed the robust formation of a large-scale *equatorial current sheet* (ECS) that emerges at and beyond the light cylinder⁷ (I. Contopoulos et al. 1999; A. N. Timokhin 2006; A. Spitkovsky 2006; C. Kalapotharakos & I. Contopoulos 2009; C. Kalapotharakos et al. 2012). In this inherently dissipative structure, magnetic reconnection and particle acceleration can naturally take place (Y. E. Lyubarskii 1996; J. G. Kirk et al. 2002; X.-N. Bai & A. Spitkovsky 2010; I. Contopoulos & C. Kalapotharakos 2010; J. Pétri 2011).

To incorporate magnetospheric dissipation and its observational implications, the FF framework was extended into the so-called *FIDO* model (Force-Free Inside, Dissipative Outside), introduced by C. Kalapotharakos et al. (2014) (see also G. Brambilla et al. 2015; C. Kalapotharakos et al. 2017). This model introduced a finite plasma conductivity zone outside the light cylinder, enabling particle acceleration and tunable energy dissipation. It was shown to reproduce the general characteristics of LAT gamma-ray light curves and, more importantly, provided a natural setting for the location of the high-energy emission within the ECS. Importantly, C. Kalapotharakos et al. (2014) found that the effective ECS emissivity is not uniform but instead concentrated in specific regions (closer to the rotational equator) along the sheet, which plays a key role in setting the observed pulse morphologies. Notably, by assuming that the radio emission originates near the magnetic poles at low altitudes, C. Kalapotharakos et al. (2014) successfully reproduced the observed correlation between radio phase lag δ and gamma-ray pulse profile peak separation Δ for LAT YPs. This phase agreement localizes the gamma-ray emission to the ECS outside the light cylinder and, together with the resulting non-uniform ECS emissivity, provides a strong geometric constraint on the emission zones.

Further refinement of pulsar emission modeling came through kinetic, three-dimensional global Particle-in-Cell (PIC) simulations (e.g., A. A. Philippov & A. Spitkovsky 2014; A. A. Philippov et al. 2015; B. Cerutti et al. 2016; G. Brambilla et al. 2018; C. Kalapotharakos et al. 2018; A. A. Philippov & A. Spitkovsky 2018; C. Kalapotharakos et al. 2023), which self-consistently evolve both the electromagnetic fields and the particle distributions across the entire magnetosphere⁸. These simulations suggest that the dominant high-energy emission originates in the ECS, where particles are accelerated to the highest Lorentz factors and emit either curvature or synchrotron radiation, primarily beyond the light cylinder.

A key regulating factor in these global PIC simulations is the rate of pair injection in the so-called *separatrix zone* (SZ), a narrow region near the boundary separating open and closed field lines, where plasma is presumably supplied to the broader ECS by unresolved magnetospheric cascades. The SZ controls the level of local dissipation and, consequently, determines both the gamma-ray luminosity and the spectral cutoff energy of the pulsar emission (C. Kalapotharakos et al. 2023, see also C. Kalapotharakos et al. 2017).

In parallel, a deeper yet relatively simple theoretical insight led to the identification of a striking empirical correlation now known as the *Fundamental Plane* (FP) of gamma-ray pulsars using phase-averaged observables. Using a sample of 88 pulsars from the Second Fermi Pulsar Catalog (A. A. Abdo et al. 2013), C. Kalapotharakos et al. (2019) showed that the gamma-ray luminosity L_γ scales with the measured spectral cutoff energy ϵ_c , the surface magnetic field B_* , and the spin-down power $\dot{\mathcal{E}}$ as

$$L_\gamma \propto \epsilon_c^{1.18 \pm 0.24} B_*^{0.17 \pm 0.05} \dot{\mathcal{E}}^{0.41 \pm 0.08}, \quad (1)$$

a relation consistent with theoretical expectations for curvature radiation in the ECS beyond the light cylinder. In this regime, the relevant radius of curvature is dimensionally set by length scales associated with the light cylinder, thereby coupling the global magnetospheric structure geometry to the radiative process.

This FP relation was later refined in C. Kalapotharakos et al. (2022) using a larger pulsar sample from the 4FGL-DR3 catalog, yielding

$$L_\gamma = 10^{14.3 \pm 1.3} \epsilon_c^{1.39 \pm 0.17} B_*^{0.12 \pm 0.03} \dot{\mathcal{E}}^{0.39 \pm 0.05}, \quad (2)$$

where ϵ_c is measured in MeV, B_* is measured in G, and $\dot{\mathcal{E}}$ and L_γ are measured in erg s^{-1} and was further corroborated by PIC simulations in C. Kalapotharakos et al. (2023), where the quantities extracted directly from the particle distributions and radiation calculations, rescaled to realistic pulsars, reproduced both the theoretical FP scaling and the observed trends in the LAT data.

⁷ The light cylinder is the cylindrical surface where the corotation speed equals the speed of light, defined by $R_{LC} = c/\Omega$, with Ω the stellar angular velocity.

⁸ These global PIC models, however, do not capture realistic field strengths, self-consistent relativistic plasma injection from polar-cap pair cascades, or the actual high Lorentz factors achieved near the ECS, making rescaling or extrapolation schemes necessary.

A complementary validation of the FP was provided by [E. O. Anguner \(2025\)](#), who analyzed pulsars from the third LAT pulsar catalog ([D. A. Smith et al. 2023](#), 3PC, hereafter) and used machine-learning techniques on the radio-loud population to estimate distances for radio-quiet gamma-ray pulsars. Their study confirmed that the FP is favored as a gamma-ray pulsar luminosity function (for sources with significant spectral cutoffs), effectively ruling out synchrotron emission as the dominant process in the LAT band.

Taken together, these investigations consolidate the FP as a physically grounded and observationally verified framework, strengthened by numerical simulations. They strongly support the interpretation that the high-energy emission in LAT pulsars originates from curvature radiation in the ECS, with the key phase-averaged observables and pulsar parameters (L_γ , ϵ_c , $\dot{\mathcal{E}}$, and B_*) linked by underlying physics rather than selection effects.

Additional insight can be drawn from the observed pulsar population, beyond the LAT detections. While the FP is applicable across a wide parameter space, the observed gamma-ray pulsars occupy only a limited portion of it. Clearly, the FP relation breaks down when $\dot{\mathcal{E}} < L_\gamma$. Since $d \log L_\gamma / d \log \dot{\mathcal{E}} < 1$ in Eq. 1–2, simple energy conservation implies the existence of a threshold $\dot{\mathcal{E}}$ below which these relations no longer apply⁹.

But what is the form of L_γ at low $\dot{\mathcal{E}}$? For higher $\dot{\mathcal{E}}$, simulations suggest that high-energy emission could be possible in areas of the FP where no pulsars have yet been detected, which suggests additional physics not yet captured by these models. This raises key questions: Why do gamma-ray pulsars populate only a specific region of the FP? Does this reflect observational biases, or does it point to intrinsic physical boundaries (such as gamma-ray death lines or death valleys) defined either in terms of spin-down power $\dot{\mathcal{E}}$ or more complex conditions within the FP itself? In this work, we aim to explore these questions and characterize the physical constraints that determine the visibility and viability of pulsed gamma-ray emission across neutron stars.

In this work, we investigate the physical origins of the FP’s regime of applicability. We argue that the confinement of observed pulsars to a limited region arises from the presence of a gamma-ray *death border*. By this we mean the upper envelope in FP space defined jointly by the *maximal radiation-reaction-limited* (RRLmax) and *potential-drop-limited* (PDL) branches. This boundary is not a single line but a finite-width band: for a given $\dot{\mathcal{E}}$, different combinations of P and B_* yield slightly different theoretical envelopes, which collectively form the practical “death border.” The location and shape of this death border are set in part by the evolution of the maximum achievable spectral cutoff energies and by the transition from the RRLmax regime to the PDL regime, where acceleration is governed by the available rotationally driven voltage. These constraints influence the detectability of pulsars, particularly at lower $\dot{\mathcal{E}}$ values, and lead us to examine the existence of an undetected population of MeV-bright pulsars that likely lie below the LAT sensitivity threshold. More broadly, the same competition between radiation-reaction limits and a finite available voltage should also arise in other current-sheet accelerators beyond isolated pulsars, for example, in the dynamically interacting magnetospheres of merging binary neutron stars ([D. Skiathas et al. 2025](#)).

Together with the distribution of observed gamma-ray pulsars on the FP, our results provide a comprehensive framework for understanding the phase-averaged gamma-ray emission of pulsars, highlighting the role of pair-production efficiency, set by intrinsic pulsar properties such as B_* and rotation period P , in regulating which pulsars can sustain bright MeV-GeV emission. At the same time, while the FP and RRL scalings capture most of the Fermi-LAT population, the highest- $\dot{\mathcal{E}}$ sources do not follow the RRLmax track indefinitely: their spectral cutoff energies, ϵ_c , flatten relative to the envelope, indicating additional screening of the accelerating electric field component, E_{acc} . This plausibly arises from enhanced pair creation in the ECS (or in other magnetospheric regions that supply pairs to the ECS), which modulates the effective accelerating scale. To explore a physical trigger for this behavior, we introduce a compactness-based criterion for optically thin $\gamma\gamma$ pair feedback (e^\pm creation) in or near the ECS and discuss its population-level implications. As an extension of the same activation picture, we also outline the possible opening of the $\gamma\gamma \rightarrow \mu^\pm$ channel and the corresponding prospects for pulsed multi-TeV neutrinos in the most energetic systems. We also quantify this e^\pm pair-regulated deviation and its implications for population visibility and spectra.

Our findings also indicate that distinct visibility thresholds may apply to YPs and MSPs, motivating us to extend our analysis to other classes of neutron stars such as magnetars and transitional high-B pulsars, most of which have thus far eluded GeV gamma-ray detection. We show that some high-B pulsars lie near the gamma-ray detection threshold, suggesting that rotation-powered ECS emission peaking in the MeV band may occur in certain high- $\dot{\mathcal{E}}$ magnetars. This component would coexist with magnetically-powered inner magnetospheric emission from resonant Compton scattering in some magnetars ([M. G. Baring & A. K. Harding 2007](#); [M. G. Baring et al. 2011](#); [A. M. Beloborodov 2013](#); [Z. Wadiasingh et al. 2018, 2019](#); [A. K. Harding et al. 2025](#)). Future MeV-sensitive instruments with phase-resolved spectropolarimetric capabilities might be able to disentangle these distinct magnetically and rotationally powered emission components.

⁹ These efficiency arguments, based on the voltage-like scaling of L_γ , imply a lower bound $\dot{\mathcal{E}} \sim \text{few} \times 10^{32} \text{ erg/s}$ below which bright gamma-ray emission is untenable; this was first noted by [J. Arons \(1996\)](#) for EGRET pulsars.

Finally, we turn our attention to the recent remarkable detection of pulsed TeV emission from the Vela pulsar phase-aligned with the LAT GeV component (A. Djannati-Ataï 2022; H. E. S. S. Collaboration et al. 2023). To assess whether this component can be understood within the same physical framework, we connect our theoretical and computational models with these observations. Using particle energy distributions from our PIC simulations, combined with a simplified prescription of the target photon field, we investigate how inverse Compton (IC) spectra evolve with the magnetospheric particle population. Our goal is to determine whether both the GeV and TeV emission from Vela can be explained self-consistently through the ECS-residing particle population.

The paper is organized as follows. In Section 2, we develop the theoretical framework, deriving the RRLmax and PDL branches, the transition $\dot{\mathcal{E}}$, and the resulting ϵ_c and L_γ scalings (including parameter-dependence through dimensionless scale factors). Section 3 confronts these scalings with 3D PIC results, projecting models onto the FP, quantifying degeneracies among effective scaling factors, and comparing YP and MSP branches. In Section 4, we map the framework to observations: we place Australia Telescope National Facility (ATNF; R. N. Manchester et al. 2005)¹⁰ pulsars and McGill magnetars (S. A. Olausen & V. M. Kaspi 2014)¹¹ on the projected FP, derive a practical gamma-ray visibility threshold on the P - \dot{P} diagram, and identify the MeV-bright/GeV-faint corridor relevant to next-generation MeV missions. In Section 5, we extend to TeV energies, using (rescaled) PIC particle distributions plus a simple seed-photon prescription to explore IC components and their consistency with Fermi-LAT and H.E.S.S. observations of Vela. Finally, Section 6 summarizes our main conclusions, synthesizes the results, introduces a compactness-based criterion for in-situ $\gamma\gamma \rightarrow e^\pm$ pair creation, contrasts the curvature-ECS and synchrotron viewpoints, and outlines implications, open questions, and (as an exploratory extension) the prospects for pulsed multi-TeV neutrino emission via $\gamma\gamma \rightarrow \mu^\pm$.

2. DEATH BORDER ON THE FP

In this section, we identify and characterize gamma-ray death lines and emission regimes, examining how they arise from basic radiative constraints and how they manifest on the FP.

2.1. Radiation reaction limit

The characteristic spectral cutoff energy in the curvature radiation limit, ϵ_c , is given by (J. D. Jackson 1998)

$$\epsilon_c = \frac{3c\hbar\gamma_L^3}{2R_c}, \quad (3)$$

where γ_L is the Lorentz factor of the emitting particle and R_c the corresponding radius of curvature.

In the RRL regime of continuous losses, the rate of energy gain from the accelerating electric field balances the radiative energy losses. This condition reads:

$$\dot{\gamma}_{\text{acc}} = \dot{\gamma}_{\text{loss}} \\ \frac{q_e c \eta_{B_{\text{LC}}} B_{\text{LC}}}{m_e c^2} = \frac{2q_e^2 \gamma_L^4}{3m_e c R_c^2}, \quad (4)$$

where q_e and m_e are the electron charge and mass, c is the speed of light, B_{LC} is the magnetic field at the light cylinder, and $\eta_{B_{\text{LC}}}$ is the accelerating electric field, E_{acc} (in units of B_{LC}).

Assuming a radius of curvature $R_c = \eta_{R_{\text{LC}}} R_{\text{LC}}$ (with $R_{\text{LC}} = P c / (2\pi)$ the light cylinder radius), and $B_{\text{LC}} = B_\star r_\star^3 / R_{\text{LC}}^3$ where B_\star and r_\star are the stellar surface magnetic field and radius respectively, and using the expression for the spin-down power in dipolar force-free (FF) magnetospheres

$$\dot{\mathcal{E}} = \eta_\alpha \frac{16\pi^4 B_\star^2 r_\star^6}{c^3 P^4}, \quad (5)$$

with P the stellar period and $\eta_\alpha \approx 1 + \sin^2 \alpha$ modulating the FF spin-down as a function of the magnetic inclination angle α (A. Spitkovsky 2006; C. Kalapotharakos & I. Contopoulos 2009; J. Pétri 2012; A. Tchekhovskoy et al. 2013), ranging from ≈ 1 (aligned rotator) to ≈ 2 (orthogonal rotator), one can derive from Eq. 4 the Lorentz factor in the RRL regime, $\gamma_{\text{L,RRL}}$:

$$\gamma_{\text{L}}^{\text{RRL}} = \left(\frac{3\pi r_\star^3 B_\star}{q_e c P} \right)^{1/4} \eta_{B_{\text{LC}}}^{1/4} \eta_{R_{\text{LC}}}^{1/2} \\ \approx 5.1 \times 10^7 \eta_{B_{\text{LC}}}^{1/4} \eta_{R_{\text{LC}}}^{1/2} r_6^{3/4} B_{12}^{1/4} P_{-1}^{-1/4}, \quad (6)$$

¹⁰ <https://www.atnf.csiro.au/research/pulsar/psrcat>

¹¹ <http://www.physics.mcgill.ca/~pulsar/magnetar/main.html>

where $B_{12} = B_\star/10^{12}$ G, $P_{-1} = P/0.1$ s, and $r_6 = r_\star/10^6$ cm. Note the weak dependence on B_{12} and P_{-1} .

Substituting back into Eq. 3, the corresponding maximum spectral cutoff energy in the RRL regime is:

$$\begin{aligned}\epsilon_c^{\text{RRL}} &= \frac{3^{7/4} \hbar c^{9/16} \dot{\mathcal{E}}^{7/16}}{2^{7/4} q_e^{3/4} r_\star^{3/8} B_\star^{1/8}} \eta_{B_{\text{LC}}}^{1/2} \eta_{B_{\text{LC}}}^{3/4} \eta_\alpha^{-7/16} \\ &\approx 10.2 \eta_{B_{\text{LC}}}^{1/2} \eta_{B_{\text{LC}}}^{3/4} \eta_\alpha^{-7/16} \dot{\mathcal{E}}_{36}^{7/16} B_{12}^{-1/8} r_6^{-3/8} \text{ GeV},\end{aligned}\quad (7)$$

where $\dot{\mathcal{E}}_{36} = \dot{\mathcal{E}}/10^{36}$ erg s $^{-1}$. The dependence of ϵ_c^{RRL} on $\dot{\mathcal{E}}$ and B_\star had been demonstrated in C. Kalapotharakos et al. (2017) but without the details regarding the scaling factors.

Finally, we note that the generic RRL relations above are valid for any $\eta_{B_{\text{LC}}}$, while the RRLmax regime is defined by setting $\eta_{B_{\text{LC}}} = \eta_{B_{\text{LC}}}^{\text{max}}$, the largest value compatible with a quasi-FF global magnetospheric structure. This choice yields the upper-envelope Lorentz factors, γ_L^{RRLmax} , and cutoff energies, $\epsilon_c^{\text{RRLmax}}$, that define the death-border.

2.2. Available Potential Drop

Equation 7 holds under the assumption that particles can reach the Lorentz factor given by Eq. 6. However, the maximum energy that particles can attain is constrained by the available potential drop they experience and the energy losses they incur along their entire trajectory through the magnetosphere, up to the point where they emit gamma-rays.

Assuming that particles are accelerated by a fraction η_{pc} of the total potential drop available at the polar cap (taken to be that of an aligned, $\alpha = 0^\circ$, force-free rotator), the maximum attainable Lorentz factor, provided it remains below the RRL, is given by

$$\begin{aligned}\gamma_L^{\text{PDL}} &= \eta_{\text{pc}} \frac{q_e B_{\text{LC}} R_{\text{LC}}}{m_e c^2} \\ &= \eta_{\text{pc}} \frac{4\pi^2 q_e r_\star^3 B_\star}{m_e c^4 P^2} \approx 2.6 \times 10^9 r_6^3 B_{12} P_{-1}^{-2}.\end{aligned}\quad (8)$$

Substituting Eq. 8 into Eq. 3 yields the corresponding maximum cutoff energy:

$$\begin{aligned}\epsilon_c^{\text{PDL}} &= \frac{3\hbar q_e^3}{2m_e^3 c^{27/4}} \frac{\eta_{\text{pc}}^3}{\eta_{B_{\text{LC}}} \eta_\alpha^{7/4}} \frac{\dot{\mathcal{E}}^{7/4}}{r_\star^{3/2} B_\star^{1/2}} \\ &\approx 2.8 \times 10^6 \text{ GeV} \cdot r_6^{-3/2} \dot{\mathcal{E}}_{36}^{7/4} B_{12}^{-1/2} \eta_{\text{pc}}^3 \eta_{B_{\text{LC}}}^{-1} \eta_\alpha^{-7/4}.\end{aligned}\quad (9)$$

While these values appear large at first glance, we will show below that the strong dependence on the spin-down power $\dot{\mathcal{E}}$ significantly reduces the expected cutoff energies for pulsars with lower $\dot{\mathcal{E}}$.

2.3. Transition Between Regimes

The analysis above implies two limiting branches for the maximum attainable particle energy: a curvature-loss RRL branch and a PDL branch such that $\gamma_L \sim \min(\gamma_L^{\text{PDL}}, \gamma_L^{\text{RRLmax}})$. For the *death-border envelope* we are specifically interested in the transition between the RRLmax realization and the PDL branch. The envelope transition occurs when the two limiting Lorentz factors are equal:

$$\begin{aligned}\gamma_L^{\text{RRLmax}} &= \gamma_L^{\text{PDL}} \\ \left(\frac{3\pi r_\star^3 B_\star}{q_e c P} \right)^{1/4} \eta_{B_{\text{LC}}}^{1/4} \eta_{B_{\text{LC}}}^{1/2} &= \eta_{\text{pc}} \frac{4\pi^2 q_e r_\star^3 B_\star}{m_e c^4 P^2},\end{aligned}\quad (10)$$

where, for notational simplicity, we henceforth write $\eta_{B_{\text{LC}}}$ to mean $\eta_{B_{\text{LC}}}^{\text{max}}$ whenever we refer to the death-border (RRLmax) envelope, unless stated otherwise.

Solving this expression and using Eq. 5, we find that the transition occurs at the following spin-down power:

$$\begin{aligned}\dot{\mathcal{E}}_{\text{TR}} &= \left(\frac{3m_e^4 c^{39/4}}{2q_e^5} \right)^{4/7} r_\star^{6/7} B_\star^{2/7} \eta_{B_{\text{LC}}}^{8/7} \eta_{B_{\text{LC}}}^{4/7} \eta_{\text{pc}}^{-16/7} \eta_\alpha \\ &\approx 7.3 \times 10^{31} \text{ erg s}^{-1} \cdot r_6^{6/7} B_{12}^{2/7} \eta_{B_{\text{LC}}}^{8/7} \eta_{B_{\text{LC}}}^{4/7} \eta_{\text{pc}}^{-16/7} \eta_\alpha.\end{aligned}\quad (11)$$

Unless explicitly stated otherwise, $\dot{\mathcal{E}}_{\text{TR}}$ denotes the *envelope* transition computed for RRLmax, i.e., with $\eta_{B_{\text{LC}}} = \eta_{B_{\text{LC}}}^{\text{max}}$.

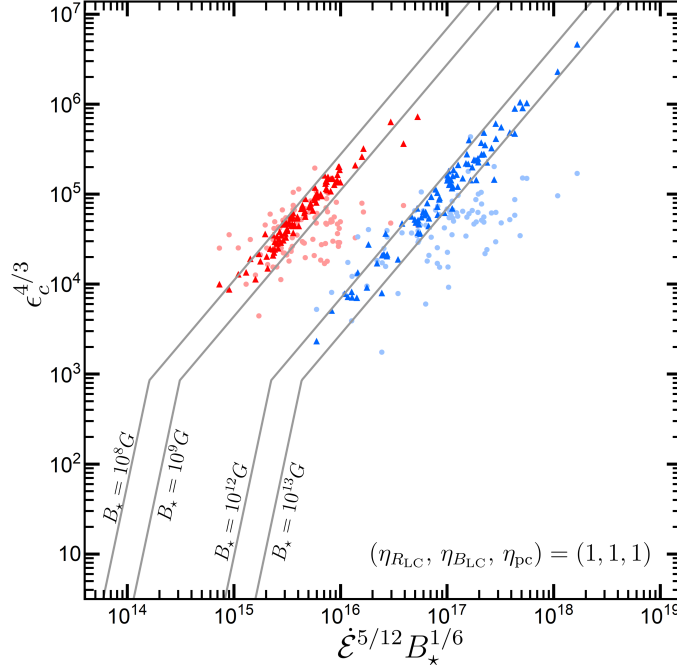


Figure 1. Projected FP of Fermi-detected gamma-ray pulsars. Light-blue filled circles: MSPs; light-red filled circles: YPs, compiled from C. Kalapotharakos et al. (2022). Dark-blue and dark-red triangles show, for the same objects, the locations obtained by adopting the theoretical maximum cutoff energies ϵ_c from Eqs. 7 and 9 with $\eta_{B_{LC}} = \eta_{R_{LC}} = \eta_{pc} = 1$, $r_* = 10^6$ cm, and $\eta_\alpha = 3/2$. Gray curves indicate loci of the death lines, i.e., maximum ϵ_c along RRL and potential-drop limited regimes, for constant surface field $B_* = 10^8, 10^9, 10^{12}, 10^{13}$ G values. The “knees” along the curves mark the transition from the maximum RRL to the potential-drop-limited branch (see Eqs. 11 and 12). Throughout this and all subsequent FP projections, ϵ_c , $\dot{\mathcal{E}}$, and B_* are expressed in MeV, erg s⁻¹, and G, respectively. *Note:* For the adopted scaling factors, the theoretical (triangle) locations are effectively deterministic and depend mainly on the measured $\dot{\mathcal{E}}$ and B_* . By contrast, the catalog-based cutoff proxy values used for the circles inherit the spectral-fit uncertainties and parameter covariances. Individual cutoff error bars are omitted for clarity; for the vast majority of sources, the quoted cutoff uncertainties are $\lesssim 0.3$ dex (often substantially smaller).

This result indicates that along the death-border envelope, for $\dot{\mathcal{E}} \lesssim \dot{\mathcal{E}}_{\text{TR}}$ the maximum cutoff energy follows the PDL branch set by the available potential drop, whereas for $\dot{\mathcal{E}} \gtrsim \dot{\mathcal{E}}_{\text{TR}}$ it follows the RRLmax branch (i.e., the upper-envelope RRL scaling). This transition sets a natural power scale and boundary in the emission behavior across the pulsar population.

Using Eq. 5, we can alternatively express the transition spin-down power, $\dot{\mathcal{E}}_{\text{TR}}$, in terms of the pulsar period P

$$\begin{aligned} \dot{\mathcal{E}}_{\text{TR}} &= \left(\frac{1}{2\pi} \right)^{2/3} \left(\frac{3m_e^4 c^{21/2}}{2q_e^5} \right)^{2/3} P^{2/3} \eta_{R_{LC}}^{4/3} \eta_{B_{LC}}^{2/3} \eta_{pc}^{-8/3} \eta_\alpha \\ &\approx 1.2 \times 10^{32} \text{ erg s}^{-1} \cdot P^{2/3} \eta_{R_{LC}}^{4/3} \eta_{B_{LC}}^{2/3} \eta_{pc}^{-8/3} \eta_\alpha, \end{aligned} \quad (12)$$

which is independent of r_* and only depends on fundamental constants.

The death lines, i.e., maximum ϵ_c along RRLmax and PDL regimes, described by Eqs. 7 and 9 depend on the magnetic field strength and various scaling factors. In Fig. 1, we show a projection of the FP onto the $\dot{\mathcal{E}}^{5/12} B_*^{1/6} - \epsilon_c^{4/3}$ plane (in log – log scale), based on the FP visualization presented in Fig. 14 of C. Kalapotharakos et al. (2023). The colored circular points show the Fermi-detected pulsars using the ϵ_{c1} values compiled in C. Kalapotharakos et al. (2022) from the 4FGL-DR3 analysis (which encompasses the LAT pulsar sample used in 3PC).

Light-colored disk-shaped markers indicate the actual positions of YPs (light blue) and MSPs (light red). The darker triangular markers correspond to the ϵ_c values predicted by the theoretical death lines given by Eqs. 7 and 9, assuming

$\eta_{R_{LC}} = \eta_{B_{LC}} = \eta_{pc} = r_6 = 1$ and $\eta_\alpha = 3/2$ ¹². These triangular points are seen to approximately trace the upper envelope of the observed ϵ_c distribution.

We also include in the exact figure theoretical death lines for representative surface magnetic field strengths of $B_\star = 10^8, 10^9, 10^{12}$, and 10^{13} G, under the same assumptions. These curves illustrate how the maximum achievable cutoff energy varies with both spin-down power and magnetic field.

In the top row of Fig. 2, we illustrate the effect of varying $\eta_{R_{LC}}$. Each panel shows five curves for $\eta_{R_{LC}} = 0.3, 1, 3, 10, 30$, assuming $\eta_{B_{LC}} = \eta_{pc} = r_6 = 1$. For clarity, we show the plots for MSPs ($B_\star = 10^8$ G) and YPs ($B_\star = 10^{12}$ G) separately, with the left panel corresponding to the former and the right panel to the latter. As $\eta_{R_{LC}}$ increases, both the maximum cutoff energy ϵ_c in the RRLmax regime and the transition spin-down power $\dot{\mathcal{E}}_{TR}$ shift to higher values. Consequently, within the PDL regime and at fixed $\dot{\mathcal{E}}$, the maximum ϵ_c decreases with increasing $\eta_{R_{LC}}$. (Across the knee, the apparent trend can change simply because the operating regime changes; the statements above apply at a fixed regime.)

In the middle row, we vary $\eta_{B_{LC}}$, plotting five curves for $\eta_{B_{LC}} = 0.03, 0.1, 0.3, 1, 3$ ¹³ with $\eta_{R_{LC}} = \eta_{pc} = r_6 = 1$. Again, the left/right panels correspond to MSPs/YPs. Increasing $\eta_{B_{LC}}$ strengthens the accelerating field, raising the RRLmax ϵ_c and shifting $\dot{\mathcal{E}}_{TR}$ to higher values. The death line associated with the PDL regime remains fixed.

Finally, in the bottom row, we examine the influence of η_{pc} by showing five curves for $\eta_{pc} = 0.01, 0.03, 0.1, 0.3, 1$, with $\eta_{R_{LC}} = \eta_{B_{LC}} = r_6 = 1$. The ϵ_c^{RRLmax} is unaffected, while the transition spin-down power $\dot{\mathcal{E}}_{TR}$ decreases as η_{pc} increases. Thus, the knee shifts to lower $\dot{\mathcal{E}}$ and, correspondingly, to lower ϵ_c at the transition.

The preceding analysis makes it evident that different combinations of scaling factors can, in principle, reproduce nearly identical death-line envelopes. In practice, however, the observed behavior in real pulsars likely results from a mix of different particle populations, each characterized by distinct parameter values.

More specifically, within a given population (MSPs or YPs; i.e., fixed representative B_\star) and for fixed η_α and r_\star , a single death-line envelope implies a fixed transition spin-down power, $\dot{\mathcal{E}}_{TR}$. From Eq. 11, we then obtain $\eta_{pc} = H_1(\dot{\mathcal{E}}_{TR}) \eta_{R_{LC}}^{1/2} \eta_{B_{LC}}^{1/4}$, where H_1 depends only on $\dot{\mathcal{E}}_{TR}$. In addition the normalization of the RRL segment is set by the product $H_2 \equiv \eta_{B_{LC}} \eta_{R_{LC}}^{2/3}$. Thus, matching a specific RRL segment implies $\eta_{B_{LC}} = H_2 \eta_{R_{LC}}^{-2/3}$, which reduces the above relation to $\eta_{pc} = H_1 H_2 \eta_{R_{LC}}^{1/3}$. In the left-hand panel of Fig. 3, we plot (in log–log space) the corresponding degeneracy curves $\eta_{B_{LC}}(\eta_{R_{LC}})$ (orange) and $\eta_{pc}(\eta_{R_{LC}})$ (blue) that reproduce the reference case $(\eta_{R_{LC}}, \eta_{B_{LC}}, \eta_{pc}) = (1, 1, 0.2)$ assuming $r_6 = 1$, $\eta_\alpha = 3/2$ and the indicated B_\star values (cyan curves on the projected FP in the right-hand panel). This reference case appears to match well the trends of the currently observed data and the PIC simulations (see Fig. 5 below). The orange and blue point distributions in the left-hand panel show the sets of $(\eta_{R_{LC}}, \eta_{B_{LC}})$ and $(\eta_{R_{LC}}, \eta_{pc})$, respectively, that map into the black bands around this reference solution in the right-hand panel. While the intrinsic degeneracy limits the ability to constrain each parameter independently, the observed pulsar distribution nonetheless excludes certain combinations that are inconsistent with the empirical trends.

2.4. Gamma-ray Efficiency

One of the key assumptions underlying the FP derivation is that the number of emitting particles in the dissipative region scales (for all pulsars) as the Goldreich-Julian (GJ) number density at the light cylinder, n_{GJ-LC} , multiplied by the dissipative volume, V_d . Assuming $V_d \propto R_{LC}^3$ and $n_{GJ-LC} \propto n_{GJ\star} R_{LC}^{-3}$, where $n_{GJ\star}$ is the GJ density at the stellar surface, $n_{GJ-LC} \times V_d$ becomes independent of the light cylinder radius and depends solely on $n_{GJ\star}$.

The notable agreement between this theoretical FP relation, the one derived from observational data, and the one obtained from PIC simulations (C. Kalapotharakos et al. 2023), supports the validity of this scaling assumption. In practical terms, this implies that the number of emitting particles, when expressed in units of the GJ density at the stellar surface, remains roughly constant across the pulsar population. That is, the product $M_{em} f_V$ does not substantially vary, where M_{em} is a dimensionless emission multiplicity factor and f_V the dissipative dimensionless volume measured in R_{LC}^3 units. This steadiness implies that either both M_{em} and f_V are roughly invariant across pulsars, or that variations in one are compensated by inverse variations in the other.

Given the GJ density at the stellar surface for a quasi-aligned rotator, $n_{GJ\star} = B_\star/(c q_e P)$, together with Eqs. 5 and 3, and following the scaling argument of C. Kalapotharakos et al. (2019), we take the per-particle gamma-ray power, $L_{\gamma,1} = \dot{\gamma}_{loss} m_e c^2$ for curvature losses (Eq. 4). If the instantaneous number of emitting particles in the dissipation zone scales as¹⁴ $N_{em} = M_{em} n_{GJ-LC} V_d = M_{em} f_V n_{GJ\star} r_\star^3$, then the total luminosity is $L_\gamma = N_{em} L_{\gamma,1}$. Defining the emitting multiplicity-volume constant $C_{MV} \equiv M_{em} f_V$, this can be written compactly as $L_\gamma = C_{MV} n_{GJ\star} r_\star^3 L_{\gamma,1}$. This

¹² Throughout this work, we adopt a representative inclination angle of $\alpha = 45^\circ$. Unless otherwise stated, we therefore set $\eta_\alpha = 3/2$.

¹³ Values $\eta_{B_{LC}} > 1$ imply that the ECS and its reconnection layer extend inward of the light cylinder, i.e., the ECS originates interior of R_{LC} , (e.g., see C. Kalapotharakos et al. 2023).

¹⁴ Equivalently using the (primary) GJ particle flux from both polar caps, $q_e N_{GJ} \sim \rho_{GJ} A_{pc} c$ which yields $N_{GJ} \sim 4\pi^2 B_\star r_\star^3 / (q_e c P^2)$. If the emitting path length at the light cylinder is $\sim R_{LC}$ and so the characteristic residence time $\sim R_{LC}/c$, $N_{em} \sim \dot{N}_{GJ} R_{LC}/c \sim B_{LC} R_{LC}^2 / q_e \sim n_{GJ\star} r_\star^3$.

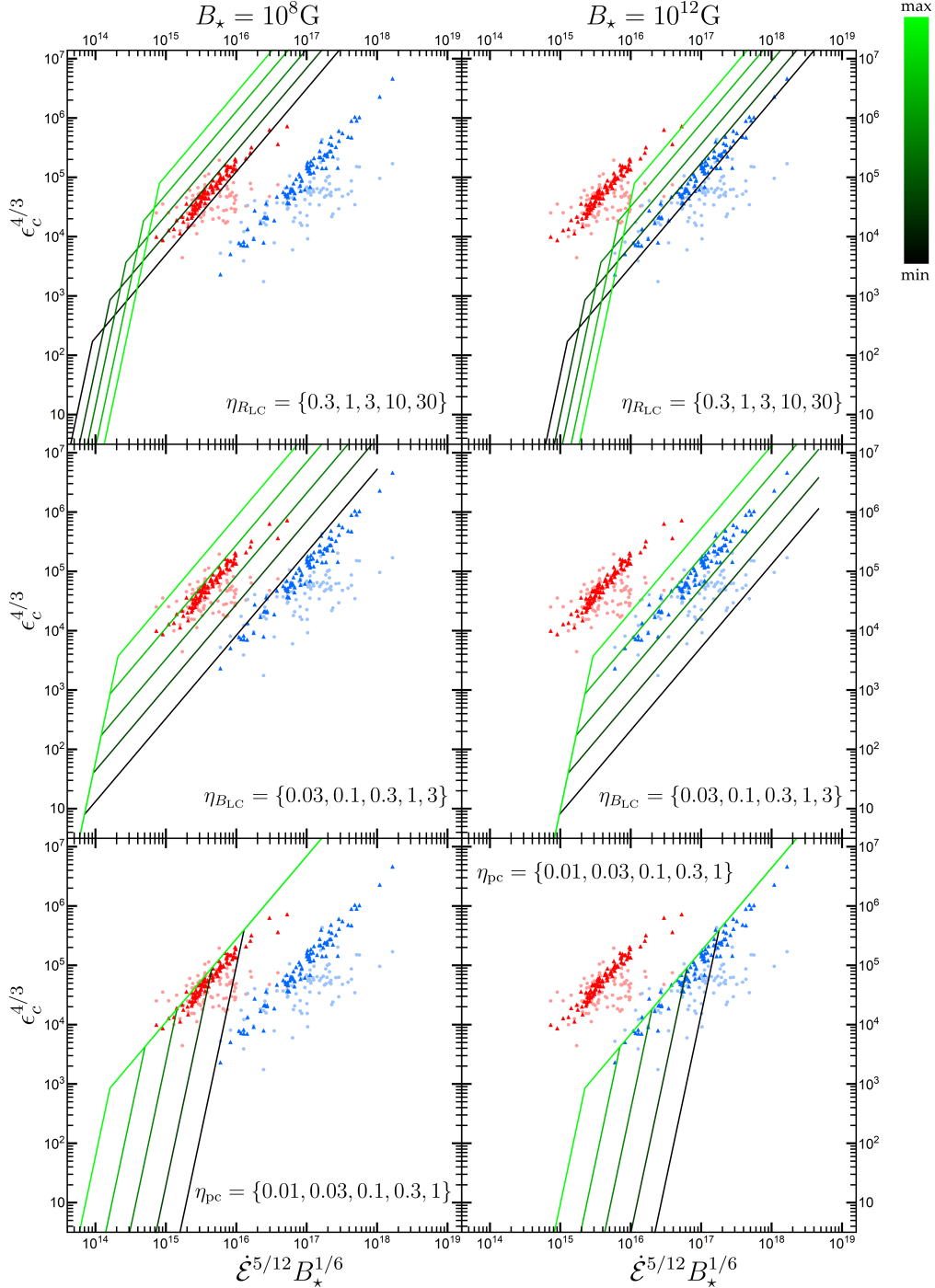


Figure 2. Projected FP for the Fermi-LAT pulsars as in Fig. 1. Each panel overlays families of death lines obtained by varying the indicated scaling factor. Left-hand column: $B_* = 10^8$ G (MSP branch). Right-hand column: $B_* = 10^{12}$ G (YP branch). The color scale indicates increasing values of the varied parameter. Except for the varied factor, all other scalings are fixed to unity, with $r_* = 10^6$ cm and $\eta_\alpha = 3/2$.

yields the quantified FP expression

$$\begin{aligned}
 L_\gamma &= C_{\text{MV}} \frac{2^{4/3} q_e r_*^{1/2}}{3^{7/3} c^{3/4} \hbar^{4/3} \pi} \eta_{R_{\text{LC}}}^{-2/3} \eta_\alpha^{-5/12} \epsilon_c^{4/3} B_*^{1/6} \dot{\mathcal{E}}^{5/12} \\
 &\approx 7.2 \times 10^4 C_{\text{MV}} r_6^{1/2} \eta_{R_{\text{LC}}}^{-2/3} \eta_\alpha^{-5/12} \epsilon_c^{4/3} B_*^{1/6} \dot{\mathcal{E}}^{5/12},
 \end{aligned} \tag{13}$$

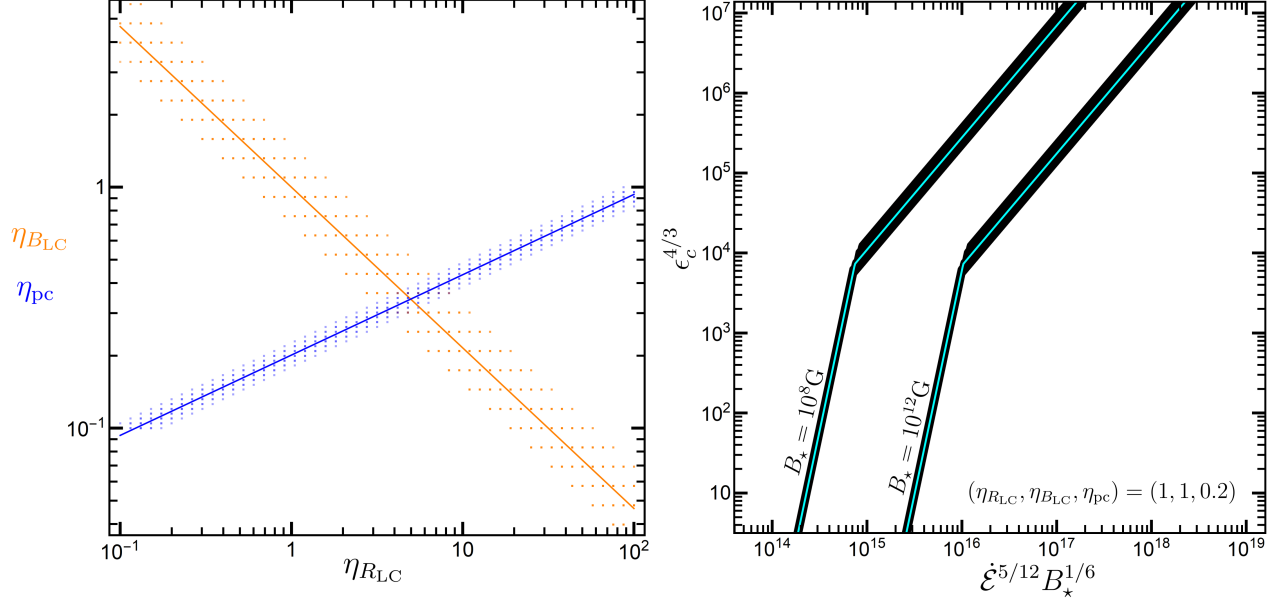


Figure 3. Left-hand panel: Degeneracy curves showing $\eta_{B_{LC}}$ (orange) and η_{pc} (blue) as functions of $\eta_{R_{LC}}$ that reproduce the same death-line envelope as the reference choice $(\eta_{R_{LC}}, \eta_{B_{LC}}, \eta_{pc}) = (1, 1, 0.2)$, which matches well the trends in the observed pulsars and the PIC simulations (see Fig. 5 below). **Right-hand panel:** The corresponding reference-case envelope is shown by the cyan curves for $\eta_\alpha = 3/2$, $r_\star = 10^6$ cm, and the indicated B_\star values. The orange and blue point distributions in the left-hand panel map onto the black bands in the right-hand panel, illustrating the range of $(\eta_{R_{LC}}, \eta_{B_{LC}}, \eta_{pc})$ combinations that are observationally degenerate around the reference solution.

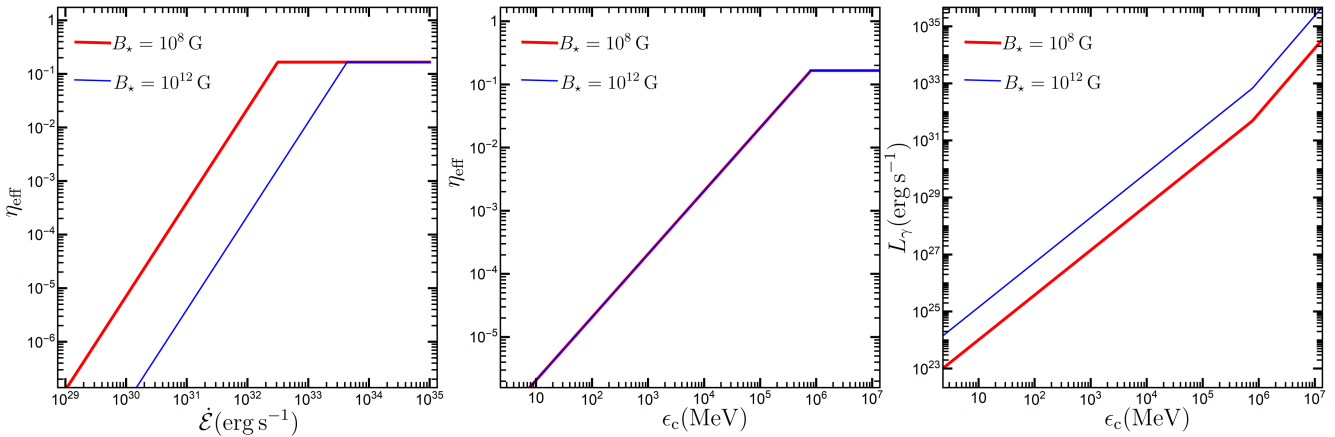


Figure 4. Behavior of gamma-ray emission across the transition from the RRL to the potential-limited regime. Each panel shows two representative curves: one for YPs ($B_\star = 10^{12}$ G, red) and one for MSPs ($B_\star = 10^8$ G, blue). Left-hand panel: gamma-ray efficiency η_{eff} as a function of $\dot{\mathcal{E}}$. Middle panel: η_{eff} versus ϵ_c (identical for YPs and MSPs). Right-hand panel: total gamma-ray luminosity L_γ as a function of ϵ_c .

where C_{MV} encapsulates the (effective) emitting multiplicity and volume. Equation 13 makes explicit the dependence on physical constants and scaling factors; the tightness of the observed FP suggests that C_{MV} varies only weakly across the pulsar population.

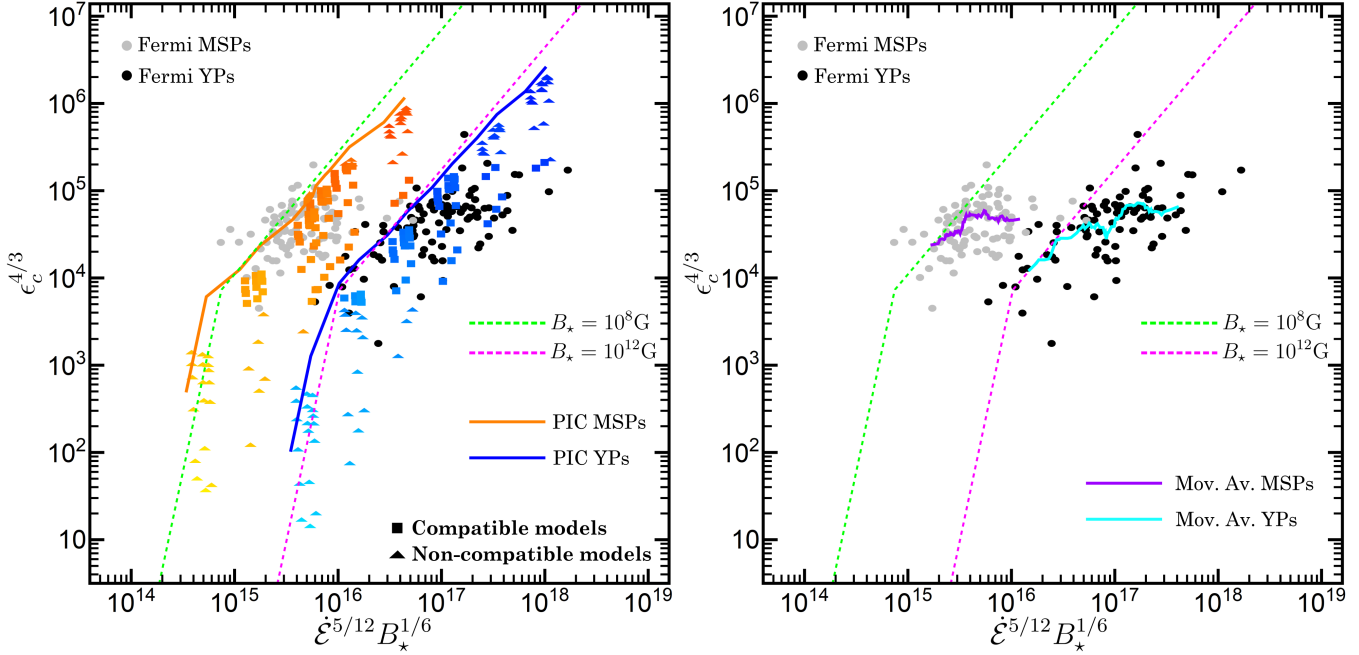


Figure 5. Left-hand panel: Projection of the FP showing Fermi-detected pulsars (gray: MSPs; black: YPs) together with the corresponding PIC model results (orange: MSPs; blue: YPs); for the PIC points, the color gradation encodes L_γ (lighter shades indicate lower L_γ , darker shades higher L_γ). Square symbols denote PIC models located within the observed FP region (compatible), while triangles indicate models without observed counterparts (non-compatible; see also C. Kalapotharakos et al. 2023). The magenta and green dashed death lines correspond to those shown as solid lines in Fig. 3 for YPs ($B_* = 10^{12}$ G) and MSPs ($B_* = 10^8$ G), respectively. The orange and blue solid lines show the theoretical death lines computed using the specific B_* and $\dot{\mathcal{E}}$ values of the PIC models. These models extend slightly below the observed range in B_* and $\dot{\mathcal{E}}$ while capturing the behavior of both emission regimes, indicating scaling factors consistent with those adopted in Fig. 3. **Right-hand panel:** Same FP projection including the Fermi pulsars and the death lines from the left-hand panel, now overlaid with the moving-average trends for the Fermi MSPs (purple) and YPs (cyan). The smoothed trends reveal that at lower $\dot{\mathcal{E}}^{5/12} B_*^{1/6}$ values the data follow the RRL branch, while at higher values they deviate from the maximal RRL regime—consistent with enhanced screening of E_{acc} and an implicit dependence of $\eta_{B_{\text{LC}}}$ on $\dot{\mathcal{E}}$.

In Eq. 13, the cutoff energy ϵ_c is expressed in eV. For consistency with the observed FP relation (Eq. 2), we convert to MeV and obtain

$$L_\gamma (\text{erg s}^{-1}) \approx 7.2 \times 10^{12} C_{\text{MV}} r_6^{1/2} \eta_{R_{\text{LC}}}^{-2/3} \eta_\alpha^{-5/12} \left(\frac{\epsilon_c}{1 \text{ MeV}} \right)^{4/3} \left(\frac{B_*}{1 \text{ G}} \right)^{1/6} \left(\frac{\dot{\mathcal{E}}}{1 \text{ erg s}^{-1}} \right)^{5/12}. \quad (14)$$

Comparing the observational FP (Eq. 2) with the theoretical expression in Eq. 14 yields $C_{\text{MV}} \propto \dot{\mathcal{E}}^{\Delta a} \epsilon_c^{\Delta b} B_*^{\Delta c}$, where Δa , Δb , and Δc denote the small differences between the corresponding FP exponents. Since the exponents in these two relations differ slightly within uncertainties, C_{MV} varies only weakly with the FP variables, i.e., it is approximately constant on the FP. This variance introduces only a mild sensitivity of C_{MV} to the specific values of L_γ , ϵ_c , B_* , and $\dot{\mathcal{E}}$.

Using representative values, $\dot{\mathcal{E}} = 10^{35} \text{ erg s}^{-1}$, $B_* = 3 \times 10^{12} \text{ G}$, and $\epsilon_c = 2 \text{ GeV}$, and equating the right-hand sides of Eqs. 2 and 14, we obtain

$$C_{\text{MV}} \approx 1.3 r_6^{-1/2} \eta_{R_{\text{LC}}}^{2/3} \eta_\alpha^{5/12}, \quad (15)$$

which implies that, for scale factors close to unity, M_{em} and f_V are approximately inversely proportional, $M_{\text{em}} \propto f_V^{-1}$.

In the RRLmax regime, corresponding to Eq. 7, the FP-based expression for the gamma-ray luminosity takes the form

$$\begin{aligned} L_\gamma^{\text{RRLmax}} &= \frac{1}{2\pi} C_{\text{MV}} \eta_{B_{\text{LC}}} \eta_\alpha^{-1} \dot{\mathcal{E}} \\ &\approx 0.21 r_6^{-1/2} \eta_{B_{\text{LC}}} \eta_{R_{\text{LC}}}^{2/3} \eta_\alpha^{-7/12} \dot{\mathcal{E}}, \end{aligned} \quad (16)$$

where, in the second line, we have applied the normalization constraint from Eq. 15. Equation 16 shows that along the RRLmax efficiency boundary, the gamma-ray efficiency $\eta_{\text{eff}} = L_\gamma/\dot{\mathcal{E}}$ is independent of $\dot{\mathcal{E}}$. For order-unity scaling factors, this gives $\eta_{\text{eff}} \sim 20\%$, consistent with the high efficiencies observed among low- $\dot{\mathcal{E}}$ pulsars. Furthermore, requiring $\eta_{\text{eff}} \leq 1$ imposes an upper bound on the combination of scaling parameters:

$$\eta_{B_{\text{LC}}} \eta_{R_{\text{LC}}}^{2/3} \eta_\alpha^{-7/12} \lesssim 4.8 r_6. \quad (17)$$

For the PDL regime corresponding to Eq. 9, the gamma-ray luminosity along the FP takes the form

$$\begin{aligned} L_{\gamma \text{pdx}} &= \frac{q_e^5}{3\pi c^{39/4} m_e^4} r_\star^{-3/2} C_{\text{MV}} \eta_{\text{pc}}^4 \eta_{R_{\text{LC}}}^{-2} \eta_\alpha^{-11/4} B_\star^{-1/2} \dot{\mathcal{E}}^{11/4} \\ &\approx 2.8 \times 10^{-51} r_6^{-3/2} C_{\text{MV}} \eta_{\text{pc}}^4 \eta_{R_{\text{LC}}}^{-2} \eta_\alpha^{-11/4} B_\star^{-1/2} \dot{\mathcal{E}}^{11/4} \\ &\approx 3.6 \times 10^{-51} r_6^{-2} \eta_{\text{pc}}^4 \eta_{R_{\text{LC}}}^{-4/3} \eta_\alpha^{-7/3} B_\star^{-1/2} \dot{\mathcal{E}}^{11/4} \\ &\approx 3.6 \times 10^{42} r_6^{-2} \eta_{\text{pc}}^4 \eta_{R_{\text{LC}}}^{-4/3} \eta_\alpha^{-7/3} B_{12}^{-1/2} \dot{\mathcal{E}}_{36}^{11/4} \end{aligned} \quad (18)$$

which implies that, along the maximum available potential drop boundary, the gamma-ray efficiency $\eta_{\text{eff}} = L_\gamma/\dot{\mathcal{E}}$ scales as $\eta_{\text{eff}} \propto \dot{\mathcal{E}}^{7/4}$. Therefore, as $\dot{\mathcal{E}}$ decreases below the transition threshold $\dot{\mathcal{E}}_{\text{TR}}$, the efficiency rapidly declines.

Figure 4 presents three panels illustrating the behavior of gamma-ray emission across the transition from the RRLmax regime to the PDL regime. Each panel includes two representative lines: one for YPs, i.e., $B_\star = 10^{12}$ G (blue) and one for MSPs, i.e., $B_\star = 10^8$ G (red).

The left-hand panel shows, in log-log scale, the total gamma-ray efficiency η_{eff} as a function of spin-down power $\dot{\mathcal{E}}$, capturing both the high-efficiency plateau in the RRLmax regime and the steep decline beyond the transition point. The middle panel displays η_{eff} as a function of the corresponding cutoff energy ϵ_c , again in log-log scale. In this case, the curves for YP and MSPs overlap, since the efficiency depends only on ϵ_c . The right-hand panel shows the actual gamma-ray luminosity L_γ as a function of ϵ_c , highlighting how the luminosity evolves as emission shifts from the RRLmax regime into the PDL regime. All panels focus on the declining part of the emission behavior but include a portion of the RRLmax regime for reference. The results assume $\eta_{R_{\text{LC}}} = \eta_{B_{\text{LC}}} = r_6 = 1$, $\eta_{\text{pc}} = 0.2$, and $\eta_\alpha = 3/2$.

The sharp decline in both ϵ_c and η_{eff} below the transition spin-down power $\dot{\mathcal{E}}_{\text{TR}}$ has essential implications for the observability of pulsars occupying this region of the FP. In Section 4, we explore this issue in greater depth, highlighting the need to develop and optimize future gamma-ray telescopes, particularly those operating in the MeV band, to access this otherwise obscured part of the pulsar population.

3. PIC SIMULATIONS: FP SCALINGS, TRANSITION, AND CONSTRAINTS

Having established the theoretical framework for gamma-ray death lines and the two distinct emission regimes, we now turn to a direct comparison between model predictions and observations on the FP. In particular, we assess how well the behavior of PIC models of pulsars aligns with the expected phase-averaged scalings and transition structure. This comparison provides a more self-consistent (3D) numerical assessment of the theoretical framework and offers insights into the physical conditions that govern the location of pulsars on the FP, including consistent numerical values of the “ η ”-scaling parameters.

In the left-hand panel of Fig. 5, we project the FP onto the $\log(\dot{\mathcal{E}}^{5/12} B_\star^{1/6})$ - $\log(\epsilon_c^{4/3})$ plane, following a similar layout to Figs. 1-3. Gray and black points (similar to light red and light blue points in Figs. 1-3) represent the Fermi-detected MSPs and YPs, respectively. The colored points correspond to PIC simulation results from (C. Kalapotharakos et al. 2023, see their Figure 14). Specifically, orange points denote model MSPs, and blue points denote model YPs. The model points extend well beyond the region populated by observed pulsars. Square markers denote models that lie within the observed pulsar region, while triangular markers represent models located in currently unobserved areas of the FP. In C. Kalapotharakos et al. (2023), the former were referred to as “compatible” and the latter as “non-compatible” models.

In the same figure, we overlay analytic curves representing characteristic scaling-factor combinations. The green and magenta lines correspond to $B_\star = 10^8$ G (MSP branch) and $B_\star = 10^{12}$ G (YP branch), respectively, using

$\eta_{R_{LC}} = 1$, $\eta_{B_{LC}} = 1$, $\eta_{pc} = 0.2$, $\eta_\alpha = 3/2$, and $r_6 = 1$. These curves provide a coarse theoretical description based on representative magnetic-field values and reproduce the general envelope of the observed and PIC model behavior. We note that an multiple combinations of $(\eta_{R_{LC}}, \eta_{B_{LC}}, \eta_{pc})$ can reproduce the same envelop (see Fig. 3).

To further demonstrate the agreement between the PIC results and the theoretical framework, we overplot in orange and blue the theoretical curves derived directly from the specific model inputs, namely, the six B_\star values and the corresponding simulation $\dot{\mathcal{E}}$ values for MSPs and for YPs in C. Kalapotharakos et al. (2023), together with their corresponding transition points $\dot{\mathcal{E}}_{TR}$. These lines do not fit the simulation data; they are obtained by evaluating the analytic relations at the simulation parameters. The close correspondence between the PIC model points and these theoretical curves reinforces the consistency of the framework and its ability to reproduce the overall scaling behavior of both pulsar populations.

The envelope formed by the highest model ϵ_c values delineates the transition between the RRLmax and PDL regimes and captures the characteristic behavior within each. In the RRLmax regime, $\epsilon_c \propto \dot{\mathcal{E}}^{7/16}$; in the PDL regime, $\epsilon_c \propto \dot{\mathcal{E}}^{7/4}$. The break between these slopes identifies the transition spin-down power, $\dot{\mathcal{E}}_{TR}$. Models lying closest to this upper envelope correspond to the lowest particle injection rates in the separatrix layer, which favor the highest achievable ϵ_c values.

In the PIC simulations, as in real pulsars, the emission arises from particle distributions that sample a range of local conditions, effectively corresponding to different scaling factors. Nevertheless, the global behavior is well captured by a set of *effective* scale factors. Because the upper envelope reproduces both the regime-specific slopes and the transition location, it encodes these effective combinations and, despite underlying parameter degeneracies, delineates robust constraints on their allowed values.

While the upper envelope of the observed pulsars' ϵ_c values appears to follow the theoretical RRLmax trend reasonably well, despite some scatter in the data, we examine this more closely in the right-hand panel of Fig. 5. For clarity, we replot the projected FP, showing the Fermi pulsars as gray circles (MSPs) and black circles (YPs), along with the theoretical guidelines (for $B_\star = 10^8$ G and $B_\star = 10^{12}$ G) from the left-hand panel.

To highlight overall trends, we overlay moving-average lines for both populations: purple for MSPs and cyan for YPs. At low $\dot{\mathcal{E}}$, these moving averages align well with the theoretical RRLmax lines. However, in both populations, we observe an apparent deviation from the RRLmax trend occurring at similar values of ϵ_c . Beyond this point, at higher $\dot{\mathcal{E}}$, the observed ϵ_c values flatten out and fall below the RRLmax envelope. Within our framework, this behavior directly implies that the effective accelerating field in the ECS does not remain at its maximal value, i.e., $\eta_{B_{LC}}$ must decrease below $\eta_{B_{LC}}^{\max}$, consistent with the onset of enhanced pair production that screens E_{acc} in the emitting/accelerating region. Quantitatively, enforcing an approximately stabilized ϵ_c above the deviation point via Eq. 7 requires $\eta_{B_{LC}} \propto \dot{\mathcal{E}}^{-7/12}$, very close to the behavior inferred in earlier ECS-based studies (e.g., C. Kalapotharakos et al. 2017, 2022). We explore and discuss the origin and implications of this deviation in Section 6.

4. OBSERVATIONAL CONSEQUENCES

Our previous analysis (e.g., see Fig. 5) indicates that the spectral ϵ_c values closely follow the maximum available ones below some spin-down power, i.e., the point where the moving average values start deviating from the RRLmax lines.

To assess how pulsar detectability by current and future gamma-ray instruments is influenced by the emission behaviors described above, we consider an *upper-limit* scenario in which all pulsars emit at their maximum achievable ϵ_c . This assumption is particularly justified at lower $\dot{\mathcal{E}}$ values, below which the observed moving-average ϵ_c matches the maximum RRLmax regime. Specifically, we considered all pulsars (~ 2750) from the ATNF catalog with recorded values of spin-down power ($\dot{\mathcal{E}}$), surface magnetic field (B_\star), period (P), and distance (d)¹⁵. For each pulsar, we computed the corresponding maximum cutoff energy (ϵ_c) using either Eq. 7 (RRLmax regime) or Eq. 9 (PDL regime), based on its $\dot{\mathcal{E}}$, assuming scaling factors of $\eta_{R_{LC}} = 1$, $\eta_{B_{LC}} = 1$, and $\eta_{pc} = 0.2$. With these calculated ϵ_c values and adopted η factors, we then derived the corresponding gamma-ray luminosity (L_γ) from Eqs. 16 and 18. Finally, using the known distances and assuming an Earth-directed beaming factor of $f_b = 1$ (R. W. Romani & K. P. Watters 2010), we calculated the corresponding gamma-ray energy flux, $F_\gamma = L_\gamma / (4\pi d^2)$, at Earth for each pulsar.

In addition to the ATNF catalog, we also included magnetars from the McGill magnetar catalog to ensure a more complete representation of the high-magnetic-field neutron star population. While some magnetars are already listed in the ATNF catalog, the McGill catalog provides an updated and dedicated compilation, albeit with a relatively small sample size (about 30 objects). Consequently, the overlap between the two catalogs is minimal and does not affect the overall statistics. Any duplicate entries were retained without modification, since they are inconsequential to the analysis.

¹⁵ These are predominantly radio-loud pulsars, as reliable distance estimates are generally unavailable for radio-quiet systems.

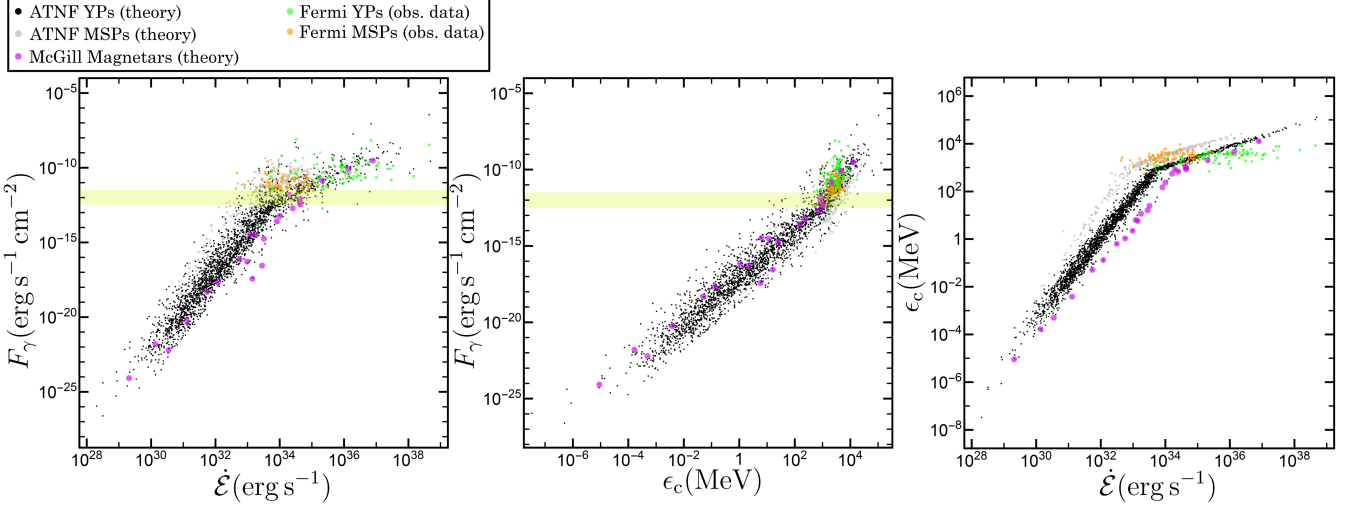


Figure 6. Left-hand panel: Predicted gamma-ray flux at Earth, F_γ , versus spin-down power, $\dot{\mathcal{E}}$, for pulsars from the ATNF catalog (gray: MSPs; black: YPs), Fermi-detected pulsars from C. Kalapotharakos et al. (2022) (orange: MSPs; green: YPs), and magnetars from the McGill catalog (magenta). For Fermi pulsars, measured F_γ values are plotted, while for ATNF pulsars and magnetars, F_γ is computed assuming L_γ values from Eqs. 16 and 18, depending on whether $\dot{\mathcal{E}}$ lies above or below $\dot{\mathcal{E}}_{\text{TR}}$ (Eq. 11), assuming a beaming factor $f_b = 1$ and the scaling factors corresponding to the death lines shown in Figs. 3 and 5. The yellow band marks the Fermi-LAT sensitivity range. **Middle panel:** F_γ versus ϵ_c . For Fermi pulsars, the reported ϵ_{c1} values (C. Kalapotharakos et al. 2022) are shown; for ATNF pulsars and magnetars, ϵ_c values are computed from the Eqs. 7 and 9 depending again on the corresponding regime. **Right-hand panel:** ϵ_c versus $\dot{\mathcal{E}}$ for the same sources, combining information from the two other panels. These diagrams illustrate the sensitivity limits and energy ranges relevant for detecting presently undetected pulsar classes. Sources predicted above the Fermi-LAT sensitivity but not detected are likely overestimated due to the assumption of the maximal RRL regime at high $\dot{\mathcal{E}}$ (see Figs. 5, 7, and text), or have unfavorable geometries that prevent their gamma-ray beams from reaching Earth.

In the left-hand panel of Fig. 6, we present a log-log plot of F_γ versus $\dot{\mathcal{E}}$. The gray and black points represent MSPs ($B_* < 10^{10}$ G) and YPs ($B_* > 10^{10}$ G), respectively, from the ATNF catalog.¹⁶ The magenta points denote magnetars from the McGill catalog. The orange and green points correspond to Fermi MSPs and YPs, respectively, taken from (C. Kalapotharakos et al. 2022). We selected the Fermi pulsar sample from C. Kalapotharakos et al. (2022), which is based on 4FGL catalog data (S. Abdollahi et al. 2022), rather than directly using 3PC, because that study derived ϵ_{c1} values, the cutoff energy parameter corresponding to a pure exponential cutoff (plus a power-law) spectral form. This parameter provides an optimal probe of the intrinsic maximum cutoff energy associated with emission from the core of the dissipative region (the ECS). It is worth noting that the underlying data in 3PC also originate from the 4FGL catalog. For the Fermi pulsars, we adopt the measured ϵ_{c1} and L_γ values, rather than the maximal emission values (corresponding to the RRLmax or PDL regimes) used for the sources in the ATNF and McGill catalogs. The transparent yellow-shaded region marks the effective sensitivity range of Fermi-LAT, approximately $10^{-11.5}$ to $10^{-12.5}$ erg cm $^{-2}$ s $^{-1}$ (which depends on sky coordinates).

The entire ATNF group clearly shows two distinct regimes: RRLmax and PDL. The Fermi pulsars lie near the RRLmax regime (and start deviating from it for larger $\dot{\mathcal{E}}$), and their flux reaches the LAT sensitivity threshold just before the knee, corresponding to the transition between the two regimes. The magnetars similarly populate both regimes; however, only three appear to lie clearly above the LAT sensitivity threshold.

In the middle and right-hand panels of Fig. 6, we show log-log plots of F_γ versus ϵ_c and ϵ_c versus $\dot{\mathcal{E}}$, respectively, using the same color coding as in the left-hand panel. Both panels reveal the two emission regimes, with their distinction most evident in the right-hand panel. In the middle panel, the LAT sensitivity threshold lies near the transition knee between the regimes. At high fluxes, within the RRLmax regime, several ATNF catalog pulsars and a few magnetars exhibit ϵ_c values at or beyond those detected by Fermi-LAT; this divergence is even more apparent in the right-hand panel, where the ATNF and magnetar ϵ_c values depart from the Fermi-LAT trend at high $\dot{\mathcal{E}}$. This behavior arises

¹⁶ In this study, we classify pulsars based on their magnetic field strength, in contrast to other works that adopt a period threshold of 30 ms. We find that using B_* provides a more effective separation of their emission properties.

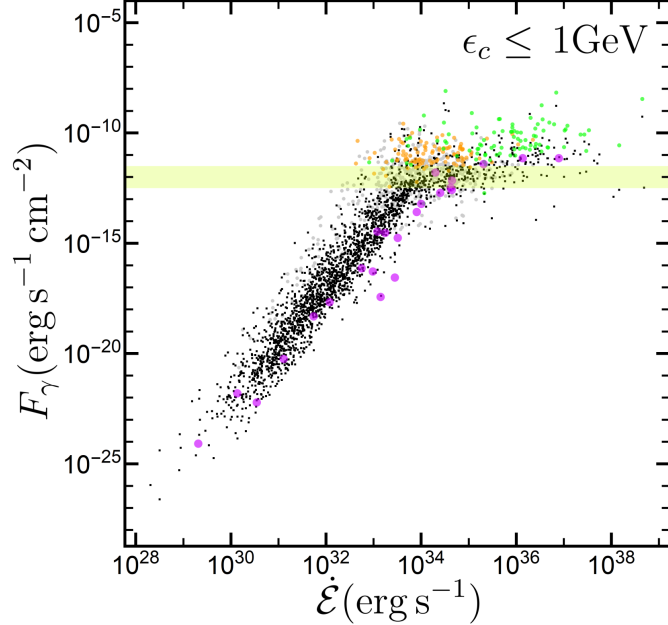


Figure 7. Same as the left-hand panel of Fig. 6, but imposing an upper limit of 1 GeV on ϵ_c to mimic the observed flattening of the cutoff energy, plausibly associated with the onset of additional pair regulation. Under this constraint, the predicted F_γ values for the highest- $\dot{\mathcal{E}}$ objects (gray, black, and magenta) are systematically reduced relative to Fig. 6, pushing them closer to (or below) detectability thresholds and making their detection more challenging.

because the ATNF and magnetar values reflect theoretical maxima. Consistent with Fig. 5, the ATNF values closely follow the RRLmax prediction at low $\dot{\mathcal{E}}$, but deviate at higher $\dot{\mathcal{E}}$, exhibiting lower ϵ_c values than those expected from the RRLmax scaling.

An important implication from these figures, and consistent with the theoretical analysis presented earlier, is that there is no intrinsic reason why MSPs and YPs should cease emitting rotation-powered high-energy radiation at lower $\dot{\mathcal{E}}$ provided plasma is able to be supplied from polar cap pair cascades, i.e., the pulsar remains above the radio death line. However, the sharp decline (below $\dot{\mathcal{E}}_{\text{TR}}$) in both ϵ_c and the corresponding lower gamma-ray efficiency, combined with the intrinsically lower $\dot{\mathcal{E}}$ values, makes the detection of high-energy emission from such pulsars increasingly difficult at low spin-down powers.

The middle column of Fig. 6 further illustrates the sensitivity requirements necessary to detect pulsars across photon energies, i.e., as a function of ϵ_c , and $\dot{\mathcal{E}}$. We emphasize, however, that these sensitivity estimates are primarily applicable to the higher- $\dot{\mathcal{E}}$ objects among the currently undetected population. It remains uncertain how far down in $\dot{\mathcal{E}}$ the same emission conditions and assumptions can be extrapolated.

Figure 6 shows that several MSPs, YPs, and possibly a few magnetars fall within the observable flux region yet remain undetected in gamma rays. Several factors could account for this. First, geometric beaming effects may prevent some radio pulsars from being observable in gamma rays, regardless of their intrinsic luminosity. While lower $\dot{\mathcal{E}}$ pulsars tend to be fainter on average, a misaligned or narrowly directed gamma-ray beam can make even intrinsically bright sources undetectable to an Earth-based observer. Second, as discussed earlier, above the characteristic transition spin-down power $\dot{\mathcal{E}}_{\text{TR}}$ for each population, pulsars may no longer operate at their maximum available ϵ_c . Although they remain in the RRL regime, increased pair-production efficiency reduces the available accelerating electric field, leading to lower ϵ_c values and, consequently, lower L_γ . While these pulsars still follow the FP relation, their L_γ reflects the reduced ϵ_c , resulting in both lower ϵ_c and reduced gamma-ray efficiency, making detection more challenging. To illustrate this effect, Fig. 7, analogous to the left-hand panel of Fig. 6, shows the expected gamma-ray fluxes for ATNF and magnetar sources with $\dot{\mathcal{E}} > \dot{\mathcal{E}}_{\text{TR}}$, assuming a fixed $\epsilon_c = 1$ GeV for all. In this scenario, most sources shift closer to, or below, the detection threshold (yellow zone).

4.1. The Gamma-Ray Visibility Threshold on the P - \dot{P} Diagram

Our analysis so far indicates that while the transition spin-down power, $\dot{\mathcal{E}}_{\text{TR}}$, is not a strict cutoff below which gamma-ray emission ceases, pulsar detectability rapidly diminishes below this point. Thus, $\dot{\mathcal{E}}_{\text{TR}}$ effectively acts as

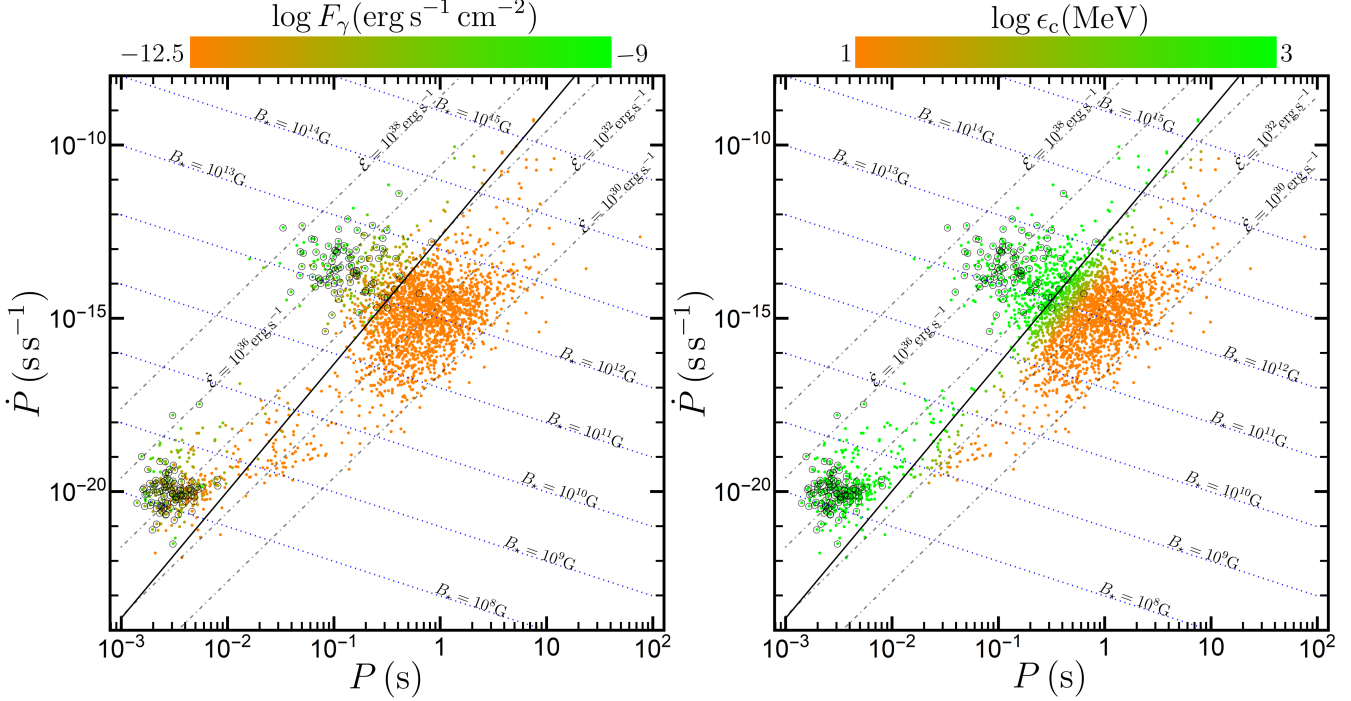


Figure 8. The P - \dot{P} diagram for all pulsars in our combined ATNF and McGill sample. Fermi-detected pulsars are marked with open circles. Blue dotted and black dot-dashed lines indicate constant B_* and \dot{E} values, respectively, while the thick black curve marks the “visibility line” where $\dot{E} = \dot{E}_{\text{TR}}$ (Eq. 20), for $\eta_{R_{\text{LC}}} = 1$, $\eta_{B_{\text{LC}}} = 1$, $\eta_{R_{\text{pc}}} = 0.2$, and $\eta_{\alpha} = 1$. The color scale shows $\log F_{\gamma}$ in the left-hand panel and $\log \epsilon_c$ in the right-hand panel. For Fermi pulsars, the observed F_{γ} and ϵ_c values are used (S. Abdollahi et al. 2020, 2022; C. Kalapotharakos et al. 2022); for the rest, these quantities are computed from Eqs. 16, 18, 7, and 9. In the left panel, both greenish and orangish points appear above the visibility line, green where sources are bright enough to be detectable, and orange where distance limits detection, while only orange points remain below it, reflecting the rapid decrease in F_{γ} and efficiency. The sole outlier, PSR J2208+4056, lies slightly below the line yet is detected (see text). In the right panel, greenish points mark sources with $\epsilon_c \gtrsim 100$ MeV, within the Fermi-LAT band. The visibility line encompasses most MSPs, bisects the YP population, and leaves magnetars below it—consistent with their non-detection in gamma rays. Where the visibility line crosses the YP locus roughly midway, the lowest-detected YPs closely track the threshold, providing empirical validation of the boundary.

an inflection point in the gamma-ray emission evolution of pulsars, marking the regime where luminosities and cutoff energies sharply decline. To clearly connect this theoretical threshold with observational parameters commonly used to classify pulsars, we explicitly derive the corresponding gamma-ray pulsar death line on the standard P - \dot{P} diagram below.

To further illustrate the implications of our findings within a familiar observational framework, we explicitly express the gamma-ray pulsar death line in terms of the standard pulsar observables P and \dot{P} . Starting from the definition of spin-down power, $\dot{E} = 4\pi^2 I_{\text{ns}} \dot{P} / P^3$ and using our previously derived transition spin-down power \dot{E}_{TR} (Eq. 12), we equate these expressions at the death line condition:

$$4\pi^2 I_{\text{ns}} \frac{\dot{P}_{\text{vis}}}{P^3} = 1.2 \times 10^{32} P^{2/3} \eta_{R_{\text{LC}}}^{4/3} \eta_{B_{\text{LC}}}^{2/3} \eta_{\text{pc}}^{-8/3} \eta_{\alpha}. \quad (19)$$

Solving explicitly for \dot{P}_{vis} and adopting the standard neutron star moment of inertia ($I_{\text{ns}} = 10^{45} \text{ g cm}^2$), we obtain the gamma-ray pulsar *visibility* line on the P - \dot{P} plane:

$$\dot{P}_{\text{vis}} \approx 3 \times 10^{-15} \eta_{R_{\text{LC}}}^{4/3} \eta_{B_{\text{LC}}}^{2/3} \eta_{\text{pc}}^{-8/3} \eta_{\alpha} P^{11/3}. \quad (20)$$

This relation provides a clear observational boundary that marks the transition between practically detectable gamma-ray pulsars and those whose emission is effectively suppressed by insufficient acceleration potential or strong radiation-reaction effects. Pulsars located below or near this line in the P - \dot{P} diagram exhibit sharply reduced gamma-ray luminosities and cutoff energies, challenging detection with current gamma-ray observatories.

In Fig. 8, we present the P – \dot{P} diagram (in log-log scale) for all pulsars in our combined ATNF and McGill sample. Both panels display the same set of objects but differ in the quantity represented by the color scale. In the left-hand panel, colors indicate the predicted gamma-ray energy flux at Earth, F_γ (corresponding to the maximum L_γ values from Eqs. 16 and 18). In contrast, in the right-hand panel, they represent the predicted spectral cutoff energy, ϵ_c (see Eqs. 7 and 9). The color scale ranges from orange to green, corresponding to $\log F_\gamma = -12.5$ to -9 in the left-hand panel and $\log \epsilon_c = 1$ to 3 (ϵ_c in MeV) in the right-hand panel, as indicated in the figure. Pulsars detected by Fermi-LAT are shown with open circles, and the solid black curve marks the gamma-ray visibility threshold derived from Eq. 20, corresponding to $\dot{\mathcal{E}} = \dot{\mathcal{E}}_{\text{TR}}$.

In the right-hand panel, greenish points mark sources with $\epsilon_c \gtrsim 100$ MeV, i.e., within the Fermi-LAT band. All but one detected pulsars lie on the observable side of the visibility curve. Greenish points that appear on the non-observable side indicate sources that could, in principle, produce > 100 MeV photons but whose predicted F_γ falls below the Fermi-LAT sensitivity, consistent with their positions and colors in the left-hand panel.

In the left-hand panel, the region above the visibility line exhibits both green and orange points: green where sources are bright enough to be detectable and orange where large distances render otherwise observable systems undetectable. Below the visibility line, we see only orange points, reflecting the rapid drop of F_γ (and, concomitantly, ϵ_c and efficiency) and the consequent lack of detections. There is one notable exception: PSR J2208+4056, which lies slightly below the line yet is detected. Its radio interpulse geometry implies an equatorial line of sight and hence a beaming factor $f_\Omega < 1$ (D. A. Smith et al. 2019), which boosts the Earthward flux relative to the $f_b = 1$ assumption used in Fig. 8. This naturally explains why J2208+4056 lies slightly below the visibility locus yet is detected by Fermi-LAT.

Where the visibility line crosses the YP locus roughly midway, the lowest-detected YPs track the threshold closely (again, with the sole outlier PSR J2208+4056 just below it), providing empirical validation of the boundary. The threshold places the vast majority of MSPs on the observable side, cuts through the YP population approximately in the middle, and leaves most magnetars on the non-observable side, consistent with their current non-detection in gamma rays.

It is important to emphasize that a pulsar’s position relative to the visibility threshold does not by itself guarantee detectability. Beaming geometry and distance are critical: green points above the line that remain undetected are plausibly due to unfavorable beaming, whereas orange points above the line are generally too distant. Conversely, below the line, there are no green points in the left-hand panel precisely because the flux drops quickly; detection would require exceptionally small distances, which are rare. In this sense, Eq. (20) defines a *necessary* condition for practical detectability, not a sufficient one. A full population-synthesis treatment that samples the underlying P – \dot{P} –distance–beaming distributions will naturally place many more MSPs and YPs above the visibility line than are currently detected, and reconciling that abundance with the modest LAT sample requires incorporating both the empirical flattening/saturation of ϵ_c at a few GeV and realistic selection effects, as explored in a companion study (M. Kerr et al. 2025).

Interestingly, we also note green-colored points (i.e., high predicted flux) above the visibility threshold that remain undetected. This subset, most notably a cluster of MSPs at high B_* and high $\dot{\mathcal{E}}$, may reflect practical limitations (e.g., orbital-period wander and eclipses in compact binaries that disrupt radio timing solutions, or a bright diffuse gamma-ray background) rather than intrinsic faintness. Improved radio timing solutions and extended ephemerides, enabling phase-coherent gamma-ray searches, could materially affect their detectability. We therefore flag these objects as priority candidates for timing follow-up and targeted Fermi-LAT pulsation searches.

As discussed above, Fig. 8 was built under an upper-limit (optimistic) assumption that each source radiates at its maximum available ϵ_c and corresponding L_γ . In practice, enhanced pair production at high B_* and high $\dot{\mathcal{E}}$ reduces the effective accelerating electric field in the ECS, lowering ϵ_c (still within the RRL regime) and thus L_γ and F_γ . This correction is most consequential for magnetars: the highest- $\dot{\mathcal{E}}$ magnetars already sit close to the visibility threshold, so any reduction in ϵ_c or L_γ readily pushes them below detectability. By contrast, high- $\dot{\mathcal{E}}$ YPs and MSPs generally lie farther above the threshold; for them, geometry (beaming) and distance typically dominate the detection outcome, with the same pair-induced suppression shifting them down but not necessarily past the threshold. When one moves from the catalog-based exercise here to a synthetic Galactic population, this saturation and suppression of ϵ_c are essential ingredients for avoiding an overabundance of predicted LAT detections at high $\dot{\mathcal{E}}$.

The significant reduction in pulsar gamma-ray luminosity and spectral cutoff energy at lower spin-down powers emphasizes the need for sensitive observational facilities in the MeV energy range. At photon energies below ~ 1 – 10 MeV, however, synchrotron components from pairs and primaries are expected to dominate the flux over the curvature component that underlies our FP-based visibility analysis (e.g., A. K. Harding & C. Kalapotharakos 2015; A. K. Harding et al. 2018, 2021). For most LAT pulsars, these synchrotron components carry a smaller fraction of the total high-energy power than the GeV curvature peak, with the Crab being a notable exception. In this low-energy

regime, synchrotron emission from primary and secondary pairs, whether produced inside the light cylinder or in the ECS reconnection layers, will generally set the observable spectrum. Thus, the visibility line derived here should be interpreted as a condition on where the high-energy ECS accelerator remains efficient and can sustain bright MeV–GeV core emission, rather than as a detailed model of the pair-synchrotron output at the lowest MeV energies.

Future telescopes, such as the planned All-sky Medium Energy Gamma-ray Observatory eXplorer (AMEGO-X) (R. Caputo et al. 2022) and the Gamma-Ray and AntiMatter Survey (GRAMS) Compton/pair telescope concept (T. Aramaki et al. 2020), are specifically designed to bridge the current observational gap between keV X-ray and GeV gamma-ray instruments. With improved sensitivity and a broader effective energy range, AMEGO-X and similar next-generation missions that utilize advanced detection technologies, such as Time Projection Chambers (TPCs) (T. Shutt et al. 2025), will be crucial both for detecting the predicted MeV-dominated, GeV-faint pulsar, magnetar, and other compact objects below the LAT sensitivity threshold and for mapping the pair-synchrotron components in already LAT-detected pulsars. Such MeV-focused missions could directly test theoretical predictions regarding emission regimes, death lines, and transitions described above, significantly enhancing our understanding of pulsar emission physics and population characteristics.

5. THE TEV PHOTON REGIME

In this section, we examine how the theoretical framework developed above, particularly as realized through our PIC simulations (C. Kalapotharakos et al. 2023), can account not only for the GeV gamma-ray emission observed by Fermi-LAT, but also for the recently discovered pulsed TeV emission from the Vela pulsar (A. Djannati-Ataï 2022; H. E. S. S. Collaboration et al. 2023). To this end, we adopt a simplified model for the target photon population, following proposals in the literature, and apply it to a set of PIC models characterized by varying degrees of force-free-ness (FF-ness). These variations yield different particle energy distributions and corresponding curvature radiation spectra. For each case, we compute the associated IC scattering spectrum and directly compare both the curvature and IC components to the observed Fermi-LAT and H.E.S.S. II spectra of Vela.

While this analysis is intended as a demonstration rather than a detailed emission model, it highlights that the framework developed in this work is not only capable of reproducing the observed GeV and TeV spectra but also appears fundamentally necessary for doing so in a self-consistent manner. The connection between curvature radiation in the ECS and IC upscattering of ambient photons emerges naturally from the structure and energetics of the PIC simulations, suggesting that a unified treatment of pulsar magnetospheric physics is essential for explaining the full extent of high-energy emission.

We calculate the IC scattering spectrum numerically via a Monte Carlo approach. The differential photon production rate due to IC scattering, expressed in the lab frame, is given by (F. C. Jones 1965; G. R. Blumenthal & R. J. Gould 1970, see also A. K. Harding & C. Kalapotharakos 2015; B. Cerutti et al. 2025):

$$\frac{dN}{dt d\epsilon_s d\epsilon_t} = \frac{2\pi r_e^2 m_e c^3}{\gamma_L^2 \epsilon_t} \left[2q_\epsilon \ln q_\epsilon + (1 + 2q_\epsilon)(1 - q_\epsilon) + \frac{1}{2} \frac{(\Gamma_\epsilon q_\epsilon)^2}{1 + \Gamma_\epsilon q_\epsilon} \right] n(\epsilon_t) \quad (21)$$

where $r_e = q_e^2/m_e c^2$ is the classical electron radius, ϵ_t and ϵ_s are the target and scatter photon energies in units of $m_e c^2$, $n(\epsilon_t) \equiv dn/d\epsilon_t$ is the differential number density of the soft photons while Γ_ϵ and q_ϵ are given by $\Gamma_\epsilon = 4\gamma_L \epsilon_t$ and $q_\epsilon = \epsilon_s/[\Gamma_\epsilon(\gamma_L - \epsilon_s)]$, respectively. The expression in Eq. 21 assumes an isotropic soft photon gas and relativistic electrons and is exact for both the Thomson ($\Gamma_\epsilon \ll 1$) and the Klein-Nishina ($\Gamma_\epsilon \gg 1$) regimes under the condition that $\gamma_L \gg 1$.

For the target photons, following A. K. Harding et al. (2018), we consider an energy distribution following a power-law

$$n(\epsilon_t) \propto \epsilon_t^{-\alpha}, \quad \epsilon_t^{\min} \leq \epsilon_t \leq \epsilon_t^{\max}, \quad (22)$$

with $\alpha = 1$ as a convenient approximation to the observed sub-millimeter to IR-optical spectrum of Vela (Y. A. Shibanov et al. 2003; A. A. Danilenko et al. 2011; D. Zyzin et al. 2013; R. P. Mignani et al. 2017; K. Liu et al. 2019) (mid-IR points are treated cautiously due to likely contamination). We set $\epsilon_t^{\min} = 0.005$ eV and $\epsilon_t^{\max} = 4$ eV to bracket the measured band.

To compute the spectrum of scattered photons, we employ the following Monte Carlo procedure: For each macroparticle in the PIC simulation, characterized by its Lorentz factor γ_L , we calculate the total probability of scattering during a time interval Δt as:

$$P_{\text{scatter}}(\gamma_L) = \Delta t \int_{\epsilon_t^{\min}}^{\epsilon_t^{\max}} \int_{\epsilon_s^{\min}}^{\epsilon_s^{\max}} \frac{dN}{dt d\epsilon_s d\epsilon_t}(\gamma_L, \epsilon_t, \epsilon_s) d\epsilon_s d\epsilon_t, \quad (23)$$

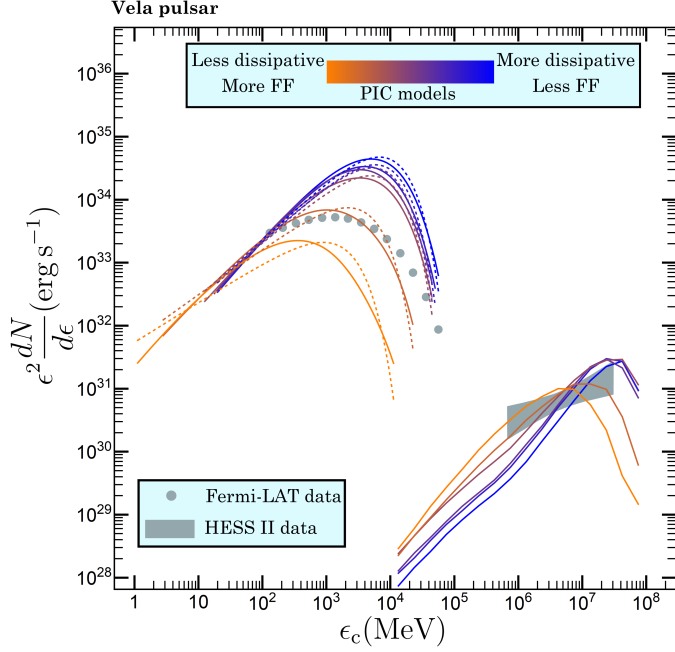


Figure 9. Curvature-radiation and IC spectra from the PIC models of C. Kalapotharakos et al. (2023) for $\alpha = 45^\circ$, compared with Fermi-LAT (gray dots) and H.E.S.S. II (gray band) data for the Vela pulsar. The PIC curvature spectra peak in the GeV range, while the IC spectra peak at TeV energies. The curve color encodes the degree of FFness: orange denotes more FF (less dissipative) models with higher particle injection rates in the separatrix zone, and blue denotes more dissipative models with lower injection rates (see C. Kalapotharakos et al. 2023 for the corresponding quantitative injection-rate values). Solid curves represent the direct PIC curvature spectra, while dashed curves show best fits (to the PIC spectra) with exponential-cutoff power laws (see C. Kalapotharakos et al. 2023 for details). The IC spectra are computed using PIC particle distributions and a uniform power-law seed-photon field. The model that best matches the Fermi-LAT spectrum also reproduces the observed H.E.S.S. shape, demonstrating a unified GeV-TeV emission framework.

where ϵ_t is the energy of the seed (target) photon and ϵ_s is the energy of the scattered photon. The limits of integration are set by $\epsilon_s^{\min} = \epsilon_t^{\min}$ and $\epsilon_s^{\max} = \gamma_L \Gamma_\epsilon / (1 + \Gamma_\epsilon)$, where Γ_ϵ is the dimensionless boost parameter relevant for the scattering kinematics (G. R. Blumenthal & R. J. Gould 1970).

In principle, using a time step Δt comparable to that of the PIC simulation yields tiny scattering probabilities, such that the number of scattered photons remains too low to construct a meaningful spectrum. To overcome this, we adopt a larger effective Δt , ensuring that $P_{\text{scatter}}(\gamma_L) < 1$ for all particles, while increasing the expected number of scattering events across the sample. For each particle, we then draw a random number $u \in [0, 1]$. If $u < P_{\text{scatter}}(\gamma_L)$, we register a scattering event and proceed to sample the scattered photon energy from the corresponding differential distribution.

For electrons that undergo scattering, we determine the scattered photon energy ϵ_s by constructing and inverting the cumulative probability distribution:

$$f_{\text{cum}}(\epsilon | \gamma_L) = \frac{1}{P_{\text{scatter}}(\gamma_L)} \int_{\epsilon_s^{\min}}^{\epsilon} \int_{\epsilon_t^{\min}}^{\epsilon_t^{\max}} \frac{dN}{dt d\epsilon_s d\epsilon_t}(\gamma_L, \epsilon_t, \epsilon_s) d\epsilon_t d\epsilon_s. \quad (24)$$

We sample ϵ_s by drawing a uniform random number and inverting this cumulative function. The resulting scattered photon energies are recorded and binned to construct the synthetic IC spectrum. Repeating this process across the entire ensemble of electrons/positrons in the PIC simulation yields a statistically robust IC spectrum that can be directly compared with observations.

In this simplified treatment, we neglect back-reaction IC energy losses on the PIC particles, since the curvature radiation losses dominate. The IC spectrum is thus computed in post-processing from the simulation's six-dimensional particle distribution function, with electron/positrons treated as test particles.

In C. Kalapotharakos et al. (2023), we explored 12 representative combinations of period (P) and surface magnetic field (B_s) spanning the parameter space occupied by YPs and MSPs. For the present analysis, we focus on the combination whose spin-down power ($\dot{\mathcal{E}}$), computed using the force-free spin-down relation (Eq. 5), is closest to that of

the Vela pulsar ($\dot{\mathcal{E}}_{\text{Vela}} \simeq 6.9 \times 10^{36} \text{ erg s}^{-1}$). This case is: ($P = 223.9 \text{ ms}$, $B_{\star} = 3.98 \times 10^{12} \text{ G}$), yielding $\dot{\mathcal{E}} \simeq 10^{37} \text{ erg s}^{-1}$. For this parameter set, six different levels of FF-ness¹⁷ were considered, corresponding to different assumptions about the pair-production efficiency in the separatrix zone.

In Fig. 9, we compare the observed phase-averaged spectrum of the Vela pulsar from Fermi-LAT and H.E.S.S. II (shown as gray data points and band) to the model spectra obtained from the selected PIC simulation. Colored curves denote different levels of FF-ness, as indicated in the legend. The model curvature radiation spectra are plotted with physically motivated normalizations, directly set by the PIC particle distributions. In contrast, the IC spectra are rescaled in overall amplitude, by adjusting the soft-photon normalization in each case, to match the observed TeV flux levels best. We find that the second-least dissipative model (dark orange curve) reproduces both the shape and normalization of the observed GeV spectrum most accurately. Remarkably, this same model also yields an IC spectrum whose shape closely matches the TeV-band observations from H.E.S.S. II, suggesting a coherent, unified explanation of the GeV and TeV emission within this framework across both energy regimes.

6. DISCUSSION AND CONCLUSIONS

6.1. Consolidated Picture and Key Results

We present a unified, observation-anchored framework for gamma-ray pulsars that ties global magnetospheric structure to population phenomenology for their phase-averaged emission. Starting from FF/FIDO insights and 3D PIC simulations, we model the ECS as the principal accelerator/emitter and derive two physically distinct operating branches for curvature radiation: an RRLmax branch and a PDL branch. These define a transition spin-down power, $\dot{\mathcal{E}}_{\text{TR}}$, and a quantified FP luminosity function. We then project ATNF pulsars and McGill magnetars onto both the FP and the $P-\dot{P}$ plane, compute (under a maximal assumption) ϵ_c , L_{γ} , and F_{γ} for each source, and compare to the Fermi-LAT sample. Finally, we assess the role of physically motivated scaling factors ($\eta_{R_{\text{LC}}}, \eta_{B_{\text{LC}}}, \eta_{\text{pc}}, \eta_{\alpha}$), identify degeneracies and constraints, show that the data deviate from the RRLmax envelope in a way suggestive of pair-regulated saturation, and demonstrate GeV-TeV consistency for Vela using PIC particle distributions plus a minimal seed-photon model. Finally, we translate these results into concrete observability forecasts, most notably a predicted MeV-dominated, GeV-faint population relevant to next-generation MeV missions.

The key results of this study are:

- (i) **Two-regime structure and scalings.** The FP envelope is set by (a) an RRLmax branch with $\epsilon_c \propto \dot{\mathcal{E}}^{7/16}$ and $L_{\gamma} \propto \dot{\mathcal{E}}$ at nearly constant efficiency, and (b) a PDL branch in which $\epsilon_c \propto \dot{\mathcal{E}}^{7/4}$ (steep rise) and the efficiency decreases (toward lower $\dot{\mathcal{E}}$) accordingly. The transition occurs at $\dot{\mathcal{E}}_{\text{TR}}$, whose scaling follows $\dot{\mathcal{E}}_{\text{TR}} \propto B_{\star}^{2/7} r_6^{6/7} \eta_{R_{\text{LC}}}^{8/7} \eta_{B_{\text{LC}}}^{4/7} \eta_{\text{pc}}^{-16/7} \eta_{\alpha} \propto P^{2/3} \eta_{R_{\text{LC}}}^{4/3} \eta_{B_{\text{LC}}}^{2/3} \eta_{\text{pc}}^{-8/3} \eta_{\alpha} \simeq 10^{32} \text{ erg s}^{-1}$ for YPs), setting a physically motivated “knee” in both ϵ_c and η_{eff} .
- (ii) **Role of scaling parameters and degeneracies.** Varying $(\eta_{R_{\text{LC}}}, \eta_{B_{\text{LC}}}, \eta_{\text{pc}})$ shifts the RRLmax envelope and $\dot{\mathcal{E}}_{\text{TR}}$ in predictable ways; different combinations can mimic similar death-line behavior. Nevertheless, the joint information of the two regime slopes and the transition location constrains viable combinations. In practice, PIC outputs are well summarized by *effective* scale factors that capture the global behavior despite underlying particle-population distributions.
- (iii) **FP normalization constrains the number of emitters.** Comparing the quantified theoretical FP relation to the observed FP exponents and normalization sets bounds on the product of emitting multiplicity and dissipative volume, $C_{\text{MV}} = M_{\text{em}} f_V \approx 1.3 r_6^{-1/2} \eta_{R_{\text{LC}}}^{2/3} \eta_{\alpha}^{5/12}$. This provides a population-level constraint on the number of particles radiating in the ECS across pulsars.
- (iv) **Visibility mapping and catalog comparison.** Mapping $\dot{\mathcal{E}}_{\text{TR}}$ onto the $P-\dot{P}$ plane defines a *gamma-ray visibility line*, i.e., $\dot{P}_{\text{vis}} \approx 3 \times 10^{-15} \eta_{R_{\text{LC}}}^{4/3} \eta_{B_{\text{LC}}}^{2/3} \eta_{\text{pc}}^{-8/3} \eta_{\alpha} P^{11/3}$. Applying this to the ATNF+McGill sample (under the maximal L_{γ} , ϵ_c assumption) and comparing with the Fermi-LAT catalog shows the expected population split: MSPs are predominantly on the observable side, YPs cluster around the boundary, and magnetars lie mostly below it. Below the line, the rapid decline of ϵ_c and F_{γ} accounts for the paucity of detections; above it, detectability is set mainly by distance, beaming geometry, and phase-coherent search depth.
- (v) **High- $\dot{\mathcal{E}}$ deviation from the RRLmax envelop and pair-regulated interpretation.** For both MSPs and YPs, the FP data reveal a clear, systematic departure of the upper ϵ_c envelop from the RRLmax scaling at

¹⁷ Here “FF-ness” parameterizes proximity to the ideal force-free state: larger FF-ness corresponds to higher particle injection in the separatrix zone, more effective screening of the accelerating electric field components, and thus less-dissipative magnetospheres; smaller FF-ness implies lower injection and more dissipative solutions (C. Kalapotharakos et al. 2023).

high $\dot{\mathcal{E}}$. More specifically, the envelope flattens and falls below the expected trend. This empirical break is a direct outcome of our analysis. In the discussion below, we show that the departure occurs at a common ϵ_c for MSPs and YPs and argue that it is naturally interpreted as the onset of pair-regulated screening in the ECS, qualitatively consistent with PIC results and compactness considerations, although a fully quantitative treatment is left for future work.

- (vi) **Magnetars and high- B pulsars: predictions and MSP follow-up.** Because the highest- $\dot{\mathcal{E}}$ magnetars sit close to the visibility line, modest additional screening (higher pair yield) can push them below detectability, consistent with their non-detections. Conversely, a characteristic subset of high- $\dot{\mathcal{E}}$, high- B_\star MSPs above the line remains undetected; targeted Fermi-LAT searches are well motivated, provided contemporaneous, phase-connected radio ephemerides are available to enable deeper phase-coherent integrations.
- (vii) **GeV-TeV unification from the ECS.** With PIC particle distributions and a minimal seed-photon field, the same ECS population that produces the GeV curvature component also yields a pulsed TeV IC component consistent in shape with Vela, without fine-tuning, supporting a clean interpretation of pulsar high-energy emission across decades in photon energy.
- (viii) **MeV-bright, GeV-faint predictions.** The framework predicts a sizeable corridor of MeV-bright, GeV-faint pulsars below current LAT sensitivity—clear targets for next-generation MeV observatories (e.g., AMEGO-X-class and TPC-based concepts), with sensitivity goals directly inferable from our FP-driven visibility analysis.

6.2. FP Interpretation: Death Border, Visibility, and Microphysics

To synthesize these results, Fig. 10 presents a schematic projection of the FP, analogous to the earlier projections: the left-hand panel shows the LAT-detected MSPs (gray points), and the right-hand panel the YPs (black points). Red regions mark parameter combinations expected to be intrinsically rare or short-lived; orange regions are forbidden by energetic and radiative constraints. The narrow cyan band labeled *death border* delineates the boundary of this forbidden domain. This band produces the characteristic knee, which currently acts as *visibility border*, i.e., the observational detection frontier with current GeV sensitivity. Just below this border lies a corridor where MeV-bright, GeV-faint pulsars are expected, despite their low gamma-ray efficiency.

Before turning to the microphysical interpretation encoded by this schematic, we note an observational caveat. A small class of “soft-gamma/MeV pulsars” are already known to be bright at hard X-ray to MeV energies while remaining weak or undetected in the GeV band (L. Kuiper & W. Hermsen 2015). Within caustic geometries in which the dominant high-energy emission arises in or near the ECS, such sources need not be in tension with the population-level picture developed here or with the broader LAT trends. If the observer line of sight samples primarily the periphery of the high-energy sky map rather than the brightest caustic core, the pulse morphology can appear single-peaked, as is common among the soft-gamma/MeV pulsars, and the observed spectrum can be biased toward lower effective cutoff energies even for relatively high $\dot{\mathcal{E}}$ (A. K. Harding & C. Kalapotharakos 2017). In our framework, this corresponds to viewing configurations that preferentially sample emission from regions with a smaller effective accelerating field and possibly a different radius of curvature, suppressing the LAT-band component while leaving a bright MeV contribution. At the same time, their concentration at high $\dot{\mathcal{E}}$ and extreme hard X-ray luminosities leaves open the possibility that their local pair yield and dissipation differ in a systematic way from the bulk LAT population, so geometry may not be the only ingredient. Distinguishing between predominantly geometric versus microphysical explanations will require phase-resolved, high-resolution forward modeling of sky maps and more sensitive MeV instruments that can substantially expand the sample of MeV-dominated pulsars, enabling sharper tests of whether these sources are geometric outliers of the same ECS-curvature sequence and placing stronger constraints on the underlying acceleration and beaming structure. With this geometric caveat in mind, we now interpret what Fig. 10 implies about pair creation and screening across the broader population.

The schematic shown in Fig. 10 encodes constraints on the pair-production microphysics, especially on magnetospheric pair-production efficiency. In the green and blue zones, our PIC-based models allow parameter values that lack detected pulsars. The interpretation is asymmetric: in the green zones, the actual pair yield is likely lower than in our (arbitrarily prescribed) injections, implying weaker screening, larger ϵ_c , and an upward shift relative to the model loci; in the blue zones, the actual pair yield is likely higher, implying stronger screening, smaller ϵ_c , and a downward shift. The interpretation naturally explains why the Fermi pulsars depart from the RRLmax envelope at higher $\dot{\mathcal{E}}$.

Although enhanced pair creation can arise in single-photon polar-cap cascades, the abrupt and nearly common departure from the RRLmax branch at similar ϵ_c might be more naturally explained by the activation of an additional site of two-photon pair production, plausibly the ECS (Y. E. Lyubarskii 1996), than by a gradual monotonic increase of polar-cap multiplicity alone (A. K. Harding & A. G. Muslimov 2011a,b; A. N. Timokhin & A. K. Harding 2015,

2019). This is especially striking because the departure appears in both YPs and MSPs, even though polar-cap pair cascades operate in quite different dynamical regimes in the two classes, with MSPs likely in the RRL regime near the polar caps (e.g. Appendix B in A. N. Timokhin & A. K. Harding 2015).

For two-photon pair creation, the Breit-Wheeler cross section for $\gamma\gamma \rightarrow e^\pm$ peaks at $\sigma_{\gamma\gamma} \sim 0.3\sigma_T$ when the two photon energies $\epsilon_{1,2}$ slightly exceed the threshold $\epsilon_1\epsilon_2(1 - \cos\theta_{12}) = 2(m_ec^2)^2$ where θ_{12} is the angle of the collision. A delta-function approximation of the cross section captures well the relevant physics and scales for nearly head-on collisions (A. A. Zdziarski & A. P. Lightman 1985). This motivates characterizing the efficacy of ECS pair production in terms of an effective photon column, i.e., a compactness parameter.

To appraise the efficacy of an additional two-photon pair-production site in the ECS, we introduce a compactness parameter (C. D. Dermer & G. Menon 2009), which quantifies the photon-energy column independently of the escape geometry. We define

$$\mathcal{C} \equiv \frac{u_\gamma \sigma_T \lambda_{\text{eff}}}{m_ec^2} = \frac{L_\gamma}{A_{\text{esc}} c} \frac{\sigma_T \lambda_{\text{eff}}}{m_ec^2} = \frac{\sigma_T L_\gamma}{m_ec^3} \frac{\lambda_{\text{eff}}}{A_{\text{esc}}}, \quad (25)$$

where u_γ is the local gamma-ray energy density, λ_{eff} is the effective length scale to escape along the photon direction within the emitting zone, and A_{esc} is the area through which those photons ultimately exit. Thus \mathcal{C} is the photon energy column $u_\gamma \lambda_{\text{eff}}$ expressed in units of m_ec^2/σ_T .

In the pulsar context, we further consider $\lambda_{\text{eff}} = \eta_\lambda R_{\text{LC}}$ and $A_{\text{esc}} = \eta_A R_{\text{LC}}^2$, with η_λ and η_A set by the emission/escape geometry (photon beaming and ECS topology). Substituting into Eq. (25) gives

$$\mathcal{C} = \frac{\sigma_T L_\gamma}{m_ec^3} \frac{\eta_\lambda}{\eta_A} \frac{1}{R_{\text{LC}}} \equiv \frac{\sigma_T L_\gamma}{m_ec^3} \frac{1}{\eta_{\text{gm}} R_{\text{LC}}}, \quad \eta_{\text{gm}} \equiv \frac{\eta_A}{\eta_\lambda}, \quad (26)$$

so that all geometric dependence is absorbed into the single factor η_{gm} (the ratio of escape area to path length in units of R_{LC} and R_{LC}^2). This formulation is agnostic to whether photons exit through faces or edges of the emitting area.

With the geometry-agnostic compactness of Eq. (26), the $\gamma\gamma$ optical depth at energy ϵ reads

$$\tau_{\gamma\gamma}(\epsilon) = \eta_s \mathcal{K}_{\gamma\gamma \rightarrow e^\pm}(\epsilon) \mathcal{C}, \quad (27)$$

where η_s is the local soft-to- γ luminosity ratio and $\mathcal{K}_{\gamma\gamma \rightarrow e^\pm}(\epsilon)$ encodes the energy/angle dependence of the $\gamma\gamma$ kernel (peaking near threshold and decreasing far above threshold). The condition $\tau_{\gamma\gamma} \gtrsim 1$ is a spectral (opacity) threshold that would imprint strong attenuation in the GeV band. Nonetheless, the FP phenomenology does not require such attenuation. The energization and screening of the ECS are governed by a dynamical activation threshold, where pair production begins to influence the accelerating electric field, E_{acc} , even in the optically thin regime, i.e., $\tau_{\gamma\gamma} \ll 1$.

In the optically thin regime, a fraction $\tau_{\gamma\gamma}$ of the GeV photons converts, and for GeV-on-keV collisions, each absorbed GeV photon produces one e^+e^- pair with Lorentz factor $\sim 10^3$. Hence, the pair injection rate is¹⁸

$$\dot{N}_{\gamma\gamma \rightarrow e^\pm} \simeq \tau_{\gamma\gamma}(\epsilon) \frac{L_\gamma}{\epsilon_c} = \eta_s \mathcal{K}_{\gamma\gamma \rightarrow e^\pm}(\epsilon) \mathcal{C} \frac{L_\gamma}{\epsilon_c}. \quad (28)$$

Defining the onset of effective pair production by the condition $\dot{N}_{\gamma\gamma \rightarrow e^\pm} \gtrsim \kappa_{\text{req}} \dot{N}_{\text{GJ}}^{(\text{PC})}$, where κ_{req} denotes the required effective multiplicity and $\dot{N}_{\text{GJ}}^{(\text{PC})} = 4\pi^2 B_\star r_\star^3 / (q_e c P^2)$ represents the Goldreich-Julian particle outflow from the polar cap, we obtain, using Eqs. 5 and 26, the corresponding condition for ϵ_c , which reads

$$\epsilon_{\text{c-thr}} = \frac{\sigma_T q_e \eta_\alpha^{1/4}}{m_ec^{15/4} r_\star^{3/2}} \frac{\eta_s \mathcal{K}_{\gamma\gamma \rightarrow e^\pm}}{\eta_{\text{gm}} \kappa_{\text{req}}} \frac{L_\gamma^2}{B_\star^{1/2} \dot{\mathcal{E}}^{1/4}}, \quad \text{with } \epsilon_c \lesssim \epsilon_{\text{c-thr}}. \quad (29)$$

Equation 29 expresses the threshold cutoff energy, $\epsilon_{\text{c-thr}}$, as a function of the accelerator observables L_γ , B_\star , and $\dot{\mathcal{E}}$, multiplied by a geometry/feedback factor $\eta_s \mathcal{K}_{\gamma\gamma \rightarrow e^\pm} / (\eta_{\text{gm}} \kappa_{\text{req}})$. The factors η_{gm} and κ_{req} , set by geometry, should not vary strongly with $\dot{\mathcal{E}}$. If, in addition, $\eta_s \mathcal{K}_{\gamma\gamma \rightarrow e^\pm}$ varies only weakly across the population below the deviation point (Fig. 5), then $\epsilon_{\text{c-thr}}$ effectively depends only on L_γ , B_\star , and $\dot{\mathcal{E}}$. A positive feedback is also expected: pair-fed synchrotron and synchrotron self-Compton (SSC) emission within the ECS increases the local soft-photon fraction η_s and broadens the spectral overlap with the GeV component, consistent with the 3PC empirical trend that higher- $\dot{\mathcal{E}}$ pulsars exhibit broader gamma-ray SEDs.

In Fig. 11 we plot the corresponding $\epsilon_{\text{c-thr}}$ loci on the projected FP for $B_\star = 10^8$ G (red; MSPs) and $B_\star = 10^{12}$ G (blue; YPs), adopting a unit modulating factor¹⁹, $\eta_s \mathcal{K}_{\gamma\gamma \rightarrow e^\pm} / (\eta_{\text{gm}} \kappa_{\text{req}}) \sim 1$. We also consider the L_γ expressions from

¹⁸ The corresponding pair rest-mass luminosity is $L_{\text{rest}} = 2m_ec^2 \dot{N}_{\gamma\gamma \rightarrow e^\pm} = (2m_ec^2/\epsilon_c) \tau_{\gamma\gamma} L_\gamma$, which for $\epsilon_c = 1$ GeV gives $L_{\text{rest}} \approx 10^{-3} \tau_{\gamma\gamma} L_\gamma$.

Eqs. 16 and 18. For reference, we overlay the right-hand panel of Fig. 5 with high transparency. The crossing where $\epsilon_c < \epsilon_{c-\text{thr}}$ occurs at nearly the same ϵ_c for both populations and coincides with the empirically inferred inflection point, consistent with a common compactness activation in the ECS that enhances pair production (and thus screening) as the RRLmax branch turns over.

Our geometry-agnostic compactness and the dynamical activation threshold in ϵ_c formalize, at the population level, the optically thin current-sheet pair feedback proposed by H. Hakobyan et al. (2019). Using local PIC simulations, they showed that even when most photons leave the upstream region unaffected, reconnection in the ECS can self-supply a co-spatial soft field and inject pairs that self-regulate the accelerator. Our suggestion extends this local picture to population data by providing a predictive condition for the cutoff-energy crossing $\epsilon_c \simeq \epsilon_{c-\text{thr}}$ on the FP and explains why MSPs and YPs depart from the maximal-RRL branch at similar ϵ_c without requiring GeV-band attenuation.

It is important to distinguish both the interaction channel and the criterion being tested. Our analysis concerns the GeV/keV channel in or near the ECS and focuses on a dynamical activation threshold (pair feedback), rather than spectral attenuation. In contrast, A. K. Harding et al. (2021) modeled the very high-energy (VHE), up to multi-TeV, IC scattering component interacting with optical-IR targets and found strong $\gamma\gamma$ attenuation for Crab but not for Vela, i.e., $\tau_{\gamma\gamma} \gg 1$ for Crab and $\tau_{\gamma\gamma} \ll 1$ for Vela. The A. K. Harding et al. (2021) results imply a small $\eta_s \mathcal{K}_{\gamma\gamma \rightarrow e^\pm}$ in the VHE/optical-IR channel for some sources, but they do not constrain the GeV/keV regime considered here, where the target photon energies and angular factors differ and where activation can occur even for $\tau_{\gamma\gamma} \ll 1$. Our geometry-agnostic compactness and the associated activation threshold therefore complement, rather than contradict, the source-specific attenuation constraints derived for the VHE band.

The compactness-based activation framework is intentionally minimal and population-level; it provides a necessary condition for ECS pair feedback and naturally captures the near-common cutoff energy at which MSPs and YPs depart from the RRLmax branch, but it is not a proof of sufficiency. Demonstrating that this mechanism operates in specific sources will require global, time-dependent kinetic radiation modeling that self-consistently couples reconnection-driven particle acceleration, anisotropic soft-photon production (synchrotron/SSC, secondary pair synchrotron, and thermal keV fields), full-angle $\gamma\gamma$ transport with relativistic aberration, and pair back-reaction on E_{acc} . Such calculations are needed to determine $\eta_s(\dot{\mathcal{E}})$, evaluate the effective kernel $\mathcal{K}_{\gamma\gamma \rightarrow e^\pm}(\epsilon)$ in the ECS geometry, constrain the geometry/current factors η_{gm} and κ_{req} , and calibrate their dispersion against source-resolved SEDs (e.g., Crab, Vela, bright MSPs). Until then, we regard \mathcal{C} and $\epsilon_{c-\text{thr}}$ as a physically motivated, testable organizing principle for the observed FP behavior, pending advanced modeling and targeted source-level validation.

6.3. Prospects for Pulsed High Energy Neutrinos From $\gamma\gamma \rightarrow \mu^\pm$

The same compactness-based activation framework can also induce the leptonic channel $\gamma\gamma \rightarrow \mu^\pm$ in or near the ECS of high- $\dot{\mathcal{E}}$ pulsars. The kinematic threshold $\epsilon_1 \epsilon_2 (1 - \cos \theta_{12}) \geq 2 m_\mu^2 c^4$ indicates that \gtrsim MeV targets can trigger muon production with GeV photons in near head-on interactions.

Similarly to before, we write the optical depth as

$$\tau_{\mu\mu}(\epsilon) = \eta_s^{(\text{MeV})} \mathcal{K}_{\gamma\gamma \rightarrow \mu^\pm}(\epsilon) \mathcal{C}, \quad (30)$$

where η_s is now the luminosity ratio between \sim MeV and GeV and $\mathcal{K}_{\gamma\gamma \rightarrow \mu^\pm}$ is the corresponding kernel for muons. Thus, the muon-pair injection rate is

$$\dot{N}_{\gamma\gamma \rightarrow \mu^\pm} \simeq \eta_s^{(\text{MeV})} \mathcal{K}_{\gamma\gamma \rightarrow \mu^\pm}(\epsilon) \mathcal{C} \frac{L_\gamma}{\epsilon_c}. \quad (31)$$

Assuming identical angular distributions and matched soft-SED shapes (normalized over their respective threshold bands) for the e^\pm and μ^\pm channels, the kernel rescales purely by the lepton mass ratio (the μ^\pm/e^\pm production cross section ratio), i.e., $\mathcal{K}_{\gamma\gamma \rightarrow \mu^\pm} = (m_e/m_\mu)^2 \mathcal{K}_{\gamma\gamma \rightarrow e^\pm}$ and so²⁰

$$\frac{\dot{N}_{\mu\mu}}{\dot{N}_{ee}} \simeq \left(\frac{m_e}{m_\mu} \right)^2 \frac{\eta_s^{(\text{MeV})}}{\eta_s^{(\text{keV})}}, \quad (32)$$

where the η_s defined in Section 6.2 is denoted with a superscript “keV” for clarity. These muons are spawned at mildly relativistic Lorentz factors.

¹⁹ The modulating factor reflects geometry, angular distributions, current-closure constraints, and the local soft-photon SED, and may vary across the population. Under plausible ECS conditions the combined factor is plausibly of order unity, but a full quantification is deferred to dedicated advanced modeling.

²⁰ Departures from identical angle/SED weighting introduce only order-unity corrections.

Subsequently, muons are further accelerated in the ECS to an average Lorentz factor $\gamma_{L\mu}$ (prior to decay). The power carried by the accelerated muon population is then

$$L_\mu \simeq 2 \gamma_{L\mu} m_\mu c^2 \dot{N}_{\mu\mu}. \quad (33)$$

Muon decays proceed primarily (S. Navas et al. 2024) via

$$\begin{aligned} \mu^+ &\rightarrow e^+ + \nu_e + \bar{\nu}_\mu, \\ \mu^- &\rightarrow e^- + \bar{\nu}_e + \nu_\mu. \end{aligned} \quad (34)$$

The decay kinematics imply that, on average, the two neutrinos take $\simeq 2/3$ of the muon energy, with characteristic mean per neutrino $\epsilon_\nu \approx (1/3) \gamma_{L\mu} m_\mu c^2$. Thus, the *pulsed* neutrino luminosity is

$$L_\nu \simeq \frac{2}{3} L_\mu = \frac{4}{3} \gamma_{L\mu} m_\mu c^2 \eta_s^{(\text{MeV})} \mathcal{K}_{\gamma\gamma \rightarrow \mu^\pm}(\epsilon) \mathcal{C} \frac{L_\gamma}{\epsilon_c}, \quad (35)$$

and the neutrino light curve should be approximately phased-aligned with the GeV/TeV γ -ray peaks.

Assuming muons experience the same available potential drop as the e^\pm and that synchrotron losses are negligible (scaling as $1/m^2$), while the curvature-reaction maximum, i.e., the RRLmax regime for muons, would require a much larger potential than available²¹, which means that the muons operate always in the PDL regime. Considering that the muons experience a fraction η_{pdm} of the available potential drop (see Equation 8), we get

$$\gamma_{L\mu} \simeq \frac{\eta_{\text{pdm}} 4\pi^2 q_e r_\star^3 B_\star}{m_\mu c^4 P^2}. \quad (36)$$

For representative LAT pulsars, the corresponding ECS acceleration time to $\gamma_{L\mu}$, i.e., $t_{\text{acc}}^\mu = \gamma_{L\mu} m_\mu c / (q_e \eta_{B_{\text{LC}}} B_{\text{LC}})$, is shorter than the lab-frame muon decay time, $\gamma_{L\mu} \tau_\mu$ (with $\tau_\mu \simeq 2.2 \mu\text{s}$), so a substantial fraction of muons can be accelerated before decaying and the resulting neutrino signal remains phase-coherent with the GeV/TeV gamma-ray emission. Substituting $\gamma_{L\mu}$ into the Eq. 35, we get

$$\frac{L_\nu}{L_\gamma} \simeq \eta_{\text{pdm}} \frac{16\pi^2 q_e r_\star^3 B_\star}{3c^2 P^2 \epsilon_c} \eta_s^{(\text{MeV})} \left(\frac{m_e}{m_\mu} \right)^2 \mathcal{K}_{\gamma\gamma \rightarrow e^\pm}(\epsilon) \mathcal{C}, \quad (37)$$

where we have also used that $\mathcal{K}_{\gamma\gamma \rightarrow \mu^\pm} = (m_e/m_\mu)^2 \mathcal{K}_{\gamma\gamma \rightarrow e^\pm}$.

Invoking the e^\pm activation condition $\eta_s^{(\text{keV})} \mathcal{K}_{\gamma\gamma \rightarrow e^\pm} / (\eta_{\text{gm}} \kappa_{\text{req}}) \simeq 1$ implied in Section 6.2 and taking into account Eq. 26, we get

$$\frac{L_\nu}{L_\gamma} \simeq \eta_{\text{pdm}} \frac{16\pi^2 q_e r_\star^3 B_\star}{3c^2 P^2 \epsilon_c} \left(\frac{m_e}{m_\mu} \right)^2 f_{\text{Mk}} \kappa_{\text{req}} \frac{\sigma_T L_\gamma}{m_e c^3 R_{\text{LC}}}, \quad (38)$$

where $f_{\text{Mk}} = \eta_s^{(\text{MeV})} / \eta_s^{(\text{keV})}$.

It follows from Eqs. 37 and 38 that the ratio L_ν/L_γ is controlled by the available potential drop (through $\gamma_{L\mu}$) and by the effective $\gamma\gamma$ optical depth for μ production $\eta_s^{(\text{MeV})} \mathcal{K}_{\gamma\gamma \rightarrow e^\pm} \mathcal{C}$; equivalently, adopting the activation condition inferred in Fig. 11, by the product $f_{\text{Mk}} \kappa_{\text{req}}$. For a representative young pulsar near the onset of enhanced $\gamma\gamma$ pair activation ($B_\star = 5 \times 10^{11} \text{ G}$, $P = 0.1 \text{ s}$, $\dot{\mathcal{E}} \approx 10^{35} \text{ erg s}^{-1}$), taking $\eta_{\text{pdm}} \simeq 0.1$ yields muons reaching $\simeq 60 \text{ TeV}$ and decay neutrinos up to $\simeq 20 \text{ TeV}$. For $L_\gamma \approx 10^{34} \text{ erg s}^{-1}$ this gives $L_\nu/L_\gamma = 10^{-3} f_{\text{Mk}} \kappa_{\text{req}}$; if $f_{\text{Mk}} \kappa_{\text{req}} \gtrsim 1$ then $L_\nu \approx 10^{31} \text{ erg s}^{-1}$. At higher $\dot{\mathcal{E}}$, the enhanced e^\pm creation reduces $\eta_{B_{\text{LC}}}$ and hence the realized potential drop, i.e., smaller η_{pdm} . Using Crab-like parameters and $\eta_{\text{pdm}} \simeq 10^{-3}$ (C. Kalapotharakos et al. 2017, 2022), one obtains $\epsilon_\nu \approx 15 \text{ TeV}$ and $L_\nu/L_\gamma \approx 10^{-2} f_{\text{Mk}} \kappa_{\text{req}}$, implying $L_\nu \gtrsim 10^{34} \text{ erg s}^{-1}$.

Alternatively, if a substantial population ($\sim 10^3$) of energetic MSPs resides in the Galactic disk and bulge, their cumulative $\gamma\gamma \rightarrow \mu^\pm$ output could contribute to the unresolved (quasi-diffuse) Galactic neutrino emission reported by IceCube (Icecube Collaboration et al. 2023). Importantly, the measured Galactic-plane signal is broadly consistent²² with diffuse neutrino production from cosmic-ray interactions in the interstellar medium, so such an MSP contribution

²¹ For muons, the RRL γ_L is the same as for e^\pm , but the corresponding energy is higher by a factor m_μ/m_e .

²² However, IceCube notes that a simple GeV-to-100 TeV extrapolation of a gamma-ray-inferred diffuse template underpredicts their best-fitting neutrino flux by a factor ~ 5 plausibly reflecting CR-transport/spectral differences toward the inner Galaxy and/or additional unresolved-source contributions.

is not required and is likely sub-dominant; nevertheless, it could still be non-negligible and would be interesting to quantify with a dedicated population-synthesis calculation (e.g., S. Tabassum & D. R. Lorimer 2025; M. Sautron et al. 2025; M. Kerr et al. 2025). MSPs have also been widely discussed as a possible contributor to the Fermi-LAT Galactic-center GeV excess, although its origin remains debated (e.g., K. N. Abazajian 2011; D. Hooper & T. Linden 2011; D. Hooper & G. Mohlabeng 2016; H. Ploeg et al. 2020; F. Calore et al. 2015; S. Manconi et al. 2024; F. List et al. 2025). In that context, constraints on (or a detection of) a neutrino component from a bulge MSP population would provide a valuable, independent handle on the viability of such scenarios.

These estimates are illustrative, grounded in a compactness-based activation scheme that provides viable interpretations of the observed phenomenology, and they define concrete, testable targets for future observations and modeling. Future observations, together with more advanced, source-resolved kinetic radiation modeling, will further constrain, and may ultimately rule out, different parameter regimes. In the near term, phase-coherent techniques using known pulsar ephemerides to suppress atmospheric and diffuse backgrounds (e.g., O. C. de Jager et al. 1989; M. Kerr 2011; J. Luo et al. 2021) might reach sensitivities to pulsed neutrino luminosities of $L_\nu \lesssim 10^{34} \text{ erg s}^{-1}$ below 50 TeV for expected bright targets (e.g., Crab) with IceCube and forthcoming facilities.

6.4. Synchrotron Narratives in the ECS

A parallel line of studies has argued that the GeV component in Fermi-detected pulsars arises predominantly from synchrotron radiation in the ECS (e.g., B. Cerutti et al. 2016; A. A. Philippov & A. Spitkovsky 2018; H. Hakobyan et al. 2023), implicitly assuming emission in fields of order B_{LC} . In that case, GeV photons can be produced with $\gamma_L \sim 10^5$ - 10^6 by reconnection alone (with the ECS magnetization as the typical limit for particle acceleration). However, such Lorentz factors are insufficient to account for the recently detected pulsed emission up to ~ 20 TeV from Vela via IC scattering: the TeV observations require $\gamma_L \gtrsim 10^{7.4}$, thereby implying particle energies well above those typically invoked in a B_{LC} -synchrotron scenario. In this sense, the TeV detection provides a decisive constraint: the emitting pairs must regularly reach $\gamma_L \gtrsim 10^7$.

In response, a branch of this literature has refined the synchrotron picture by appealing to reconnection locales with effectively small $B_\perp \ll B_{\text{LC}}$ (near X-points) and by parameterizing the outcome with the sheet magnetization σ_M (as a cap on attainable energy) and a synchrotron burnoff Lorentz factor γ_{syn} , as the cooling-limited scale (A. Chernoglazov et al. 2023). In that language, the regime is controlled by the ratio $\sigma_M/\gamma_{\text{syn}}$, and GeV cutoffs can be reached when $\sigma_M \gg \gamma_{\text{syn}}$ because particles experience acceleration in regions of reduced B_\perp . This viewpoint has gradually converged toward the FP-based picture. The two-scale competition we identified, between the curvature RRLmax, γ_L^{RRLmax} , and the PDL, γ_L^{PDL} , is directly analogous to their $(\gamma_{\text{syn}}, \sigma_M)$. The crossover condition $\sigma_M \sim \gamma_{\text{syn}}$ maps one-to-one onto our $\gamma_L^{\text{PDL}} = \gamma_L^{\text{RRLmax}}$ transition at $\dot{\mathcal{E}}_{\text{TR}}$.

We note that, in practice, the effective B_\perp sampled by the radiating particles and the dwell time spent in low- B_\perp versus radiating regions control ϵ_c . Absent a predictive mapping from global parameters to these local fractions, the degree of B_\perp reduction below B_{LC} remains model-dependent, which complicates population-level predictions compared to the curvature-ECS scalings used here.

Our framework retains this two-scale physics but anchors it to global, observable quantities. In the ECS beyond the light cylinder, the relevant curvature radius is set geometrically, $R_c \sim \eta_{\text{RLC}} R_{\text{LC}}$, so curvature emission naturally accounts for the observed GeV cutoffs with $\gamma_L \gtrsim 10^7$, and the same particle population produces the TeV component via IC scattering without further assumptions. Moreover, the curvature-ECS picture, combined with a GJ scaling of the emitter, reproduces the empirical FP exponents and yields population-level predictions (RRLmax vs. PDL branches, the transition at $\dot{\mathcal{E}}_{\text{TR}}$, and the associated visibility mapping). Beyond reproducing the FP, our framework provides explicit, testable rules for how the observables scale with spin-down power in the different regimes.

Through the “dictionary” discussed above, elements of these predictions could, in principle, be recast within the reconnection-synchrotron paradigm: their $(\sigma_M, \gamma_{\text{syn}})$ pair is the local analogue of our $(\gamma_L^{\text{PDL}}, \gamma_L^{\text{RRLmax}})$, and the regime selector $\sigma_M/\gamma_{\text{syn}}$ mirrors our $\gamma_L^{\text{PDL}}/\gamma_L^{\text{RRLmax}}$. However, turning that local description into the same FP exponents and the same $\dot{\mathcal{E}}$ -scalings for ϵ_c and L_γ requires a specific, population-wide mapping of σ_M and γ_{syn} to the global pulsar parameters $(\dot{\mathcal{E}}, B_\star, P, \alpha)$. In our curvature-ECS formulation, those scalings follow directly from the light-cylinder geometry and GJ normalization, hence the predictive power at the catalog level; in the synchrotron picture, the corresponding global closure has not yet been demonstrated and would need to recover, without fine-tuning, $\epsilon_c \propto \dot{\mathcal{E}}^{7/16}$ in the RRLmax branch and the steeper $\propto \dot{\mathcal{E}}^{7/4}$ decline in the potential-limited branch, together with the observed FP exponents.

A second practical advantage is how naturally the catalogs fit into the global picture. Projecting ATNF pulsars and McGill magnetars onto the FP and onto the $P-\dot{P}$ plane using our scalings reproduces the observed occupancy: MSPs lie predominantly on the observable side of the visibility border, YPs straddle it, and magnetars fall largely below it, with the predicted flux/cutoff behavior tracking the Fermi-LAT detections. While a reconnection-synchrotron

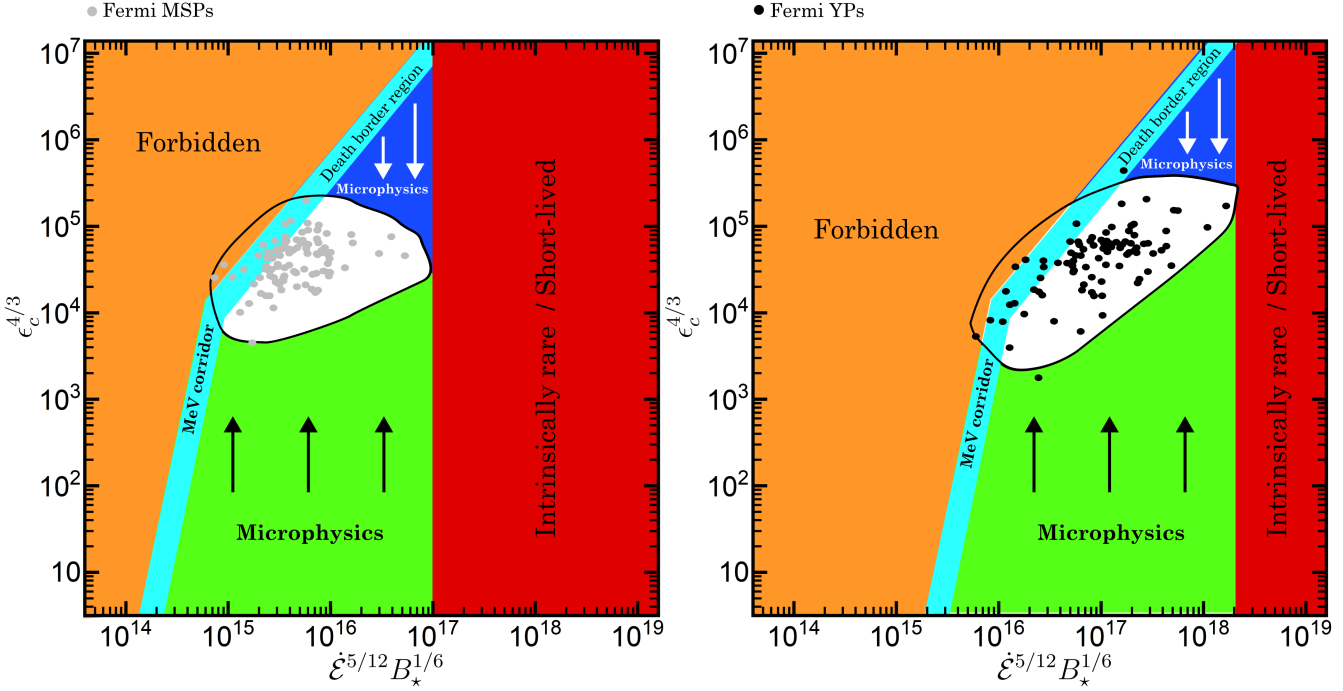


Figure 10. Projection of the FP for MSPs (left) and YPs (right), illustrating the physically distinct regions and their microphysical interpretations. Black contours enclose the observed Fermi domains. Red areas mark intrinsically rare or short-lived populations; orange zones are forbidden by energetic constraints. The cyan band delineates the death border, forming the characteristic knee that separates the maximal RRL regime from the potential-drop-limited regime. Its lower segment marks the *MeV corridor*, where MeV-bright pulsars are predicted to exist but remain challenging to detect with current instruments. The green and blue regions correspond to parameter domains where our global PIC-based models (agnostic to plasma injection microphysics) predict sources without observational counterparts. In the green zones, actual pair production is likely less efficient than in our models, implying weaker screening and higher ϵ_c values. In contrast, in the blue zones, pair production is more efficient, yielding stronger screening and lower ϵ_c values.

treatment could be made compatible via the equivalence noted above, it would similarly need to establish how σ_M and γ_{syn} co-vary with $(\dot{\mathcal{E}}, B_*, P)$ across the population so that the same visibility mapping and detection fractions emerge. In short, the two narrations share the same underlying two-scale competition; our curvature-ECS implementation ties those scales to global observables in a way that yields simple $\dot{\mathcal{E}}$ -laws and catalog-level predictions that can be, and have been, confronted directly with the data.

It is worth emphasizing that the interpretation advanced by [A. Chernoglazov et al. \(2023\)](#) effectively requires large magnetization at the light cylinder, $\sigma_M > 10^7$, in the ECS. In practice, this points to low local pair multiplicity in the emitting layer, a potentially challenging requirement for energetic pulsars such as Vela, where polar-cap pair production is expected to be substantial (e.g., [A. N. Timokhin & J. Arons 2013](#); [A. N. Timokhin & A. K. Harding 2015, 2019](#)). More generally, if the global pair yields were uniformly low, it would be challenging to sustain FF-like magnetospheres whose large-scale geometry successfully reproduces the observed gamma-ray light-curve phenomenology, (e.g., [C. Kalapotharakos et al. 2014](#)).

A natural reconciliation, consistent with our studies ([C. Kalapotharakos et al. 2017, 2018, 2019, 2022, 2023](#)), is that pair loading is spatially inhomogeneous. The overall polar-cap cascade can be high, while the multiplicity specifically along the last-open field lines that feed the ECS remains only moderate. This picture aligns with the separatrix-zone (SZ) injection framework of [C. Kalapotharakos et al. \(2023\)](#), in which the gamma-ray luminosity and cutoff are regulated by the particle injection rate into the SZ/ECS, whereas the remainder of the open field-line bundle can remain heavily pair-loaded to uphold a quasi-force-free global structure. In that sense, the high- σ_M requirement in the emitting sheet (low local multiplicity) is compatible with a globally pair-rich magnetosphere, and it maps cleanly onto the role played by the SZ injection rate in our curvature-ECS paradigm. However, this solution could run counter to the abundant local pair creation in the ECS required to moderate gamma-ray luminosity in high-spin-down-power pulsars like the Crab ([H. Hakobyan et al. 2019](#)).

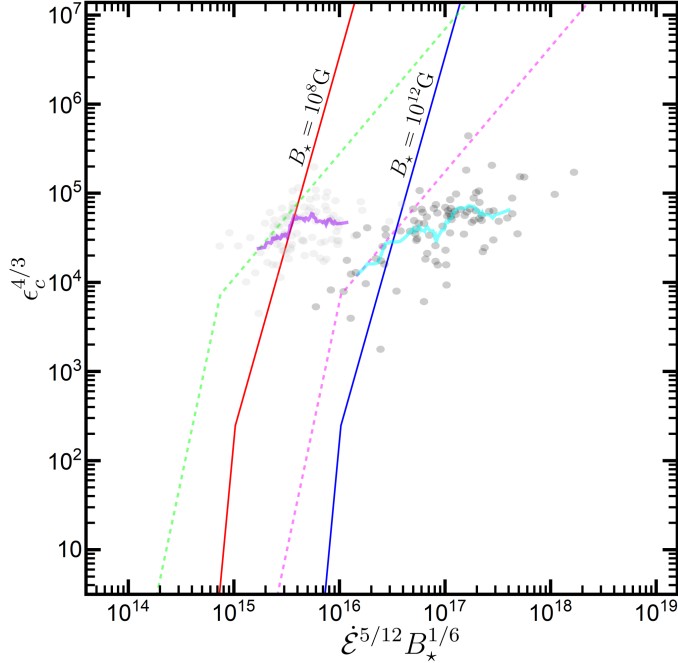


Figure 11. Loci of $\epsilon_{c\text{-thr}}$ on the projected FP for $B_* = 10^8$ G (red line; MSPs) and $B_* = 10^{12}$ G (blue line; YPs). For reference, the right-hand panel of Fig. 5 is overplotted with high transparency. The pair-activation criterion $\epsilon_c \lesssim \epsilon_{c\text{-thr}}$ is satisfied at nearly the same ϵ_c for both populations and near the observed departure from the maximal-RRL branch. This alignment, tentative but suggestive, indicates that enhanced pair creation, and the attendant screening of E_{acc} , emerge at this transition, with $\eta_{B_{\text{LC}}}$ effectively acquiring a dependence on $\dot{\mathcal{E}}$.

A second strand within the synchrotron school keeps the GeV component as synchrotron emitted in a field of order B_{LC} but posits continued acceleration for many light-cylinder radii so that the same particles subsequently reach $\gamma_{\text{L}} \gtrsim 4 \times 10^7$ and generate the TeV component by IC in the outer wind (B. Cerutti et al. 2025). This update alleviates the Vela constraint only by introducing new tensions: (i) if the LC energization is capped by the local magnetization, σ_{M} , a monotonic gain by a factor $\gtrsim 40$, at $r \gg R_{\text{LC}}$, must exceed that cap and thus relies on a specific, quantitatively characterized mechanism for sustained wind-zone acceleration, not yet developed in detail in this framework; (ii) with $B_{\perp} \propto r^{-1}$, particles at $\gamma_{\text{L}} \gtrsim 10^7$ radiate appreciable synchrotron power and retain synchrotron cutoffs $\propto \gamma_{\text{L}}^2 B_{\perp}$ out to tens-hundreds of R_{LC} , which would generally produce an additional substantial synchrotron component that is not observed unless B_{\perp} (or the pitch angle) is kept extremely small along the entire path, in which case the scenario effectively approaches large- R_c motion where the practical distinction from curvature becomes again semantic; (iii) IC luminosity gains premised on an isotropic target (e.g., the CMB) are least realistic on LC scales, while anisotropic thermal polar cap and nebular fields generally reduce the net IC yield and, being deep in the Klein-Nishina regime at $\gamma_{\text{L}} > 10^7$, further tighten the energy budget. Absent a population-level closure that maps these assumptions onto $(\dot{\mathcal{E}}, B_*, P, \alpha)$ and reproduces the FP scalings and the observed ϵ_c - L_{γ} trends without fine-tuning, this “ongoing-acceleration synchrotron” narrative remains less economical than the curvature-ECS framework, which attains $\gamma_{\text{L}} \gtrsim 10^7$ *in situ* (RRL regime), unifies the GeV and TeV components without extra wind energization, and yields direct, testable population predictions (FP exponents, $\dot{\mathcal{E}}_{\text{TR}}$, and the P - \dot{P} visibility mapping).

A related, complementary line of work models pulsar high-energy emission with an explicit synchro-curvature radiative prescription coupled to an effective (parametrized) description of particle trajectories and emission-region geometry (D. Íñiguez-Pascual et al. 2024, 2025). In these models the emitting region is assumed to lie just outside the light cylinder, close to the Y-point where the force-free condition breaks and acceleration can occur. The magnetic-field strength and curvature radius sampled by the radiating particles are treated through simple parameterizations along the trajectory rather than being taken from a global FF/PIC magnetosphere (D. Íñiguez-Pascual et al. 2025). As the particle pitch angle is rapidly damped, the emission naturally evolves toward a curvature-dominated gamma-ray component at $\gamma_{\text{L}} \gtrsim 10^7$ (D. Íñiguez-Pascual et al. 2024), which is broadly consistent with the central role for curvature emission emphasized in our ECS-based framework. At the same time, because the geometry and acceleration are

encoded through effective parameters, establishing a one-to-one mapping between those parameters and the global FF/PIC scalings across the population remains non-trivial.

6.5. Open Questions and Future Directions

The consistency between our theoretical FP scalings, the RRLmax-to-PDL transition, the P - \dot{P} visibility mapping, and the PIC model insights (including a unified account of the GeV curvature and the TeV IC components) is not the whole story. The combined theoretical and observational maturity of this paradigm now lets us pose further incisive questions, aimed at the (unresolved) microphysics that links ϵ_c , L_γ , and the GeV-TeV connection rather than phase-averaged population trends. We highlight three priorities.

- (a) **Electron-Positron yield versus P, B_* , and $\dot{\mathcal{E}}$.** Quantify the magnetospheric pair-production efficiency $\eta_{\text{pair}}(\dot{\mathcal{E}}, B_*, P, \alpha)$ that also is responsible for the observed onset of departures from the RRLmax trend. In practice, η_{pair} sets the screening of E_{acc} and thus the effective accelerating scale $\eta_{B_{\text{LC}}}$, fixing the slope change of $\epsilon_c(\dot{\mathcal{E}})$ across MSPs, YPs, and magnetars (and locating $\dot{\mathcal{E}}_{\text{TR}}$). A parallel priority is to assess how multipolar magnetic structure, especially in MSPs, where recent studies suggest significant non-dipolar components (e.g., M. C. Miller et al. 2019; T. E. Riley et al. 2019; A. Y. Chen et al. 2020; C. Kalapotharakos et al. 2021; G. Olmschenk et al. 2025), modulates η_{pair} and the resulting screening.
- (b) **PIC realism and emergent dissipation.** Global PIC is still under-resolving key scales and processes. To capture the true radiative behavior in a global magnetosphere, simulations must reach realistic magnetic fields, particle energies, and radiation-reaction strengths. Promising avenues include improved particle-orbit integrators (e.g., J. Pétri 2022), hybrid workflows that couple global MHD/FFE to embedded local PIC (e.g., A. Soudais et al. 2024), and, potentially, machine-learning surrogates that bridge current physical gaps (e.g., subgrid closures for pair yield and E_{acc} screening in global runs; super-resolution of magnetospheric structure from lower-resolution simulations; fast emulators that extrapolate particle and photon energy distributions to realistic B_* , R_{LC}/r_*) imposed by numerical limitations.
- (c) **Spectral shapes and multi-band couplings.** Beyond constraining cutoff energies, we need predictive, phase-resolved modeling of the *multiwavelength* pulsed spectrum that explains the richer 3PC spectral features and, at lower energies, the components that furnish the MeV-IR seed fields for IC. The goal is a unified framework that links the GeV curvature cutoff shape, the MeV band, and the TeV IC tail across viewing geometries, and that also predicts phase-resolved polarization signatures and time variability of the gamma-ray emission. Such a framework would tie (ϵ_c, L_γ) to $\dot{\mathcal{E}}$ in all regimes.

Looking ahead, the framework developed here provides a quantitative bridge between theory and survey design for both space- and ground-based instruments. By linking the FP scalings, the RRLmax-to-PDL transition, the observed deviation from the RRLmax regime, and the P - \dot{P} visibility mapping to observable pairs (F_γ, ϵ_c) , it defines target regions for next-generation MeV-band observatories and VHE γ -ray facilities, where phase-resolved TeV spectroscopy can test the predicted IC components. In parallel, a companion population-synthesis study builds on these scalings to model Galactic pulsar ensembles with realistic beaming/distance distributions, propagate them through instrument response functions for prospective surveys, and outline observing strategies and timing prospects, including applications to gamma-ray pulsar timing arrays (M. Kerr et al. 2025). The present work supplies the physical priors, regime structure, and visibility criteria that anchor that broader effort to detect nHz gravitational waves.

ACKNOWLEDGMENTS

We thank Alexander Philippov, Benoît Cerutti, Matthew Kerr, Regina Caputo, Abhishek Desai, Christo Venter, and George Younes for helpful discussions. We are also grateful to Liz Hays for her careful reading of the manuscript, valuable feedback, and encouragement. This material is based upon work supported by NASA under awards 80GSFC21M0002 and 80GSFC24M0006, and under grants 21-ATP21-0116, 22-ADAP22-0142, and 22-TCAN22-0027. This work is also supported by the Fermi and NICER missions. Resources supporting this work were provided by the NASA High-End Computing (HEC) Program through the NASA Advanced Supercomputing (NAS) Division at Ames Research Center. This research has made use of the NASA Astrophysics Data System.

Software: For the analysis and visualization, Mathematica (W. R. Inc. 2024) is used.

REFERENCES

Abazajian, K. N. 2011, JCAP, 2011, 010, doi: [10.1088/1475-7516/2011/03/010](https://doi.org/10.1088/1475-7516/2011/03/010) 6.3

Abdo, A. A., Ajello, M., Allafort, A., et al. 2013, ApJS, 208, 17, doi: [10.1088/0067-0049/208/2/17](https://doi.org/10.1088/0067-0049/208/2/17) 1

Abdollahi, S., Acero, F., Ackermann, M., et al. 2020, *ApJS*, 247, 33, doi: [10.3847/1538-4365/ab6bcb](https://doi.org/10.3847/1538-4365/ab6bcb) 8

Abdollahi, S., Acero, F., Baldini, L., et al. 2022, *ApJS*, 260, 53, doi: [10.3847/1538-4365/ac6751](https://doi.org/10.3847/1538-4365/ac6751) 4, 8

Anguner, E. O. 2025, *ApJ*, 985, 58 1

Aramaki, T., Adrian, P. O. H., Karagiorgi, G., & Odaka, H. 2020, *Astroparticle Physics*, 114, 107, doi: [10.1016/j.astropartphys.2019.07.002](https://doi.org/10.1016/j.astropartphys.2019.07.002) 4, 1

Arons, J. 1996, *A&AS*, 120, 49 9

Bai, X.-N., & Spitkovsky, A. 2010, *ApJ*, 715, 1282, doi: [10.1088/0004-637X/715/2/1282](https://doi.org/10.1088/0004-637X/715/2/1282) 1

Baring, M. G., & Harding, A. K. 2007, *Ap&SS*, 308, 109, doi: [10.1007/s10509-007-9326-x](https://doi.org/10.1007/s10509-007-9326-x) 1

Baring, M. G., Wadiasingh, Z., & Gonthier, P. L. 2011, *ApJ*, 733, 61, doi: [10.1088/0004-637X/733/1/61](https://doi.org/10.1088/0004-637X/733/1/61) 1

Beloborodov, A. M. 2013, *ApJ*, 762, 13, doi: [10.1088/0004-637X/762/1/13](https://doi.org/10.1088/0004-637X/762/1/13) 1

Blumenthal, G. R., & Gould, R. J. 1970, *Reviews of Modern Physics*, 42, 237, doi: [10.1103/RevModPhys.42.237](https://doi.org/10.1103/RevModPhys.42.237) 5, 5

Brambilla, G., Kalapotharakos, C., Harding, A. K., & Kazanas, D. 2015, *ApJ*, 804, 84, doi: [10.1088/0004-637X/804/2/84](https://doi.org/10.1088/0004-637X/804/2/84) 1

Brambilla, G., Kalapotharakos, C., Timokhin, A. N., Harding, A. K., & Kazanas, D. 2018, *ApJ*, 858, 81, doi: [10.3847/1538-4357/aab3e1](https://doi.org/10.3847/1538-4357/aab3e1) 1

Calore, F., Cholis, I., & Weniger, C. 2015, *JCAP*, 2015, 038, doi: [10.1088/1475-7516/2015/03/038](https://doi.org/10.1088/1475-7516/2015/03/038) 6,3

Caputo, R., Ajello, M., Kierans, C. A., et al. 2022, *Journal of Astronomical Telescopes, Instruments, and Systems*, 8, 044003, doi: [10.1117/1.JATIS.8.4.044003](https://doi.org/10.1117/1.JATIS.8.4.044003) 4,1

Cerutti, B., Figueiredo, E., & Dubus, G. 2025, *A&A*, 695, A93, doi: [10.1051/0004-6361/202451948](https://doi.org/10.1051/0004-6361/202451948) 5, 6,4

Cerutti, B., Philippov, A. A., & Spitkovsky, A. 2016, *MNRAS*, 457, 2401, doi: [10.1093/mnras/stw124](https://doi.org/10.1093/mnras/stw124) 1, 6,4

Chen, A. Y., Yuan, Y., & Vasilopoulos, G. 2020, *ApJL*, 893, L38, doi: [10.3847/2041-8213/ab85c5](https://doi.org/10.3847/2041-8213/ab85c5) (a)

Chernoglazov, A., Hakobyan, H., & Philippov, A. 2023, *ApJ*, 959, 122, doi: [10.3847/1538-4357/acffc6](https://doi.org/10.3847/1538-4357/acffc6) 6,4, 6,4

Contopoulos, I., & Kalapotharakos, C. 2010, *MNRAS*, 404, 767, doi: [10.1111/j.1365-2966.2010.16338.x](https://doi.org/10.1111/j.1365-2966.2010.16338.x) 1

Contopoulos, I., Kazanas, D., & Fendt, C. 1999, *ApJ*, 511, 351, doi: [10.1086/306652](https://doi.org/10.1086/306652) 1

Danilenko, A. A., Zyuzin, D. A., Shibanov, Y. A., & Zharikov, S. V. 2011, *MNRAS*, 415, 867, doi: [10.1111/j.1365-2966.2011.18753.x](https://doi.org/10.1111/j.1365-2966.2011.18753.x) 5

de Jager, O. C., Raubenheimer, B. C., & Swanepoel, J. W. H. 1989, *A&A*, 221, 180 6,3

Dermer, C. D., & Menon, G. 2009, *High Energy Radiation from Black Holes: Gamma Rays, Cosmic Rays, and Neutrinos* 6,2

Djannati-Ataï, A. 2022, in 31st Texas Symposium on Relativistic Astrophysics, 33 1, 5

H. E. S. S. Collaboration, Aharonian, F., Ait Benkhali, F., et al. 2023, *Nature Astronomy*, 7, 1341, doi: [10.1038/s41550-023-02052-3](https://doi.org/10.1038/s41550-023-02052-3) 1, 5

Hakobyan, H., Philippov, A., & Spitkovsky, A. 2019, *ApJ*, 877, 53, doi: [10.3847/1538-4357/ab191b](https://doi.org/10.3847/1538-4357/ab191b) 6,2, 6,4

Hakobyan, H., Philippov, A., & Spitkovsky, A. 2023, *ApJ*, 943, 105, doi: [10.3847/1538-4357/acab05](https://doi.org/10.3847/1538-4357/acab05) 6,4

Harding, A. K., & Kalapotharakos, C. 2015, *ApJ*, 811, 63, doi: [10.1088/0004-637X/811/1/63](https://doi.org/10.1088/0004-637X/811/1/63) 4,1, 5

Harding, A. K., & Kalapotharakos, C. 2017, in *Proceedings of the 7th International Fermi Symposium, held 15-20 October 2017, in Garmisch-Partenkirchen, Germany (IFS2017)*. Online at [jA href="https://pos.sissa.it/cgi-bin/reader/conf.cgi?confid=312" href="https://pos.sissa.it/cgi-bin/reader/conf.cgi?confid=312">https://pos.sissa.it/cgi-bin/reader/conf.cgi?confid=312](https://pos.sissa.it/cgi-bin/reader/conf.cgi?confid=312); <https://arxiv.org/abs/1712.02406> 6,2

Harding, A. K., Kalapotharakos, C., Barnard, M., & Venter, C. 2018, *ApJL*, 869, L18, doi: [10.3847/2041-8213/aaf3b2](https://doi.org/10.3847/2041-8213/aaf3b2) 4,1, 5

Harding, A. K., & Muslimov, A. G. 2011a, *ApJL*, 726, L10, doi: [10.1088/2041-8205/726/1/L10](https://doi.org/10.1088/2041-8205/726/1/L10) 6,2

Harding, A. K., & Muslimov, A. G. 2011b, *ApJ*, 743, 181, doi: [10.1088/0004-637X/743/2/181](https://doi.org/10.1088/0004-637X/743/2/181) 6,2

Harding, A. K., Venter, C., & Kalapotharakos, C. 2021, *ApJ*, 923, 194, doi: [10.3847/1538-4357/ac3084](https://doi.org/10.3847/1538-4357/ac3084) 4,1, 6,2

Harding, A. K., Wadiasingh, Z., & Baring, M. G. 2025, *ApJ*, 991, 178, doi: [10.3847/1538-4357/adfa06](https://doi.org/10.3847/1538-4357/adfa06) 1

Hooper, D., & Linden, T. 2011, *PhRvD*, 84, 123005, doi: [10.1103/PhysRevD.84.123005](https://doi.org/10.1103/PhysRevD.84.123005) 6,3

Hooper, D., & Mohlabeng, G. 2016, *JCAP*, 2016, 049, doi: [10.1088/1475-7516/2016/03/049](https://doi.org/10.1088/1475-7516/2016/03/049) 6,3

Íñiguez-Pascual, D., Torres, D. F., & Viganò, D. 2024, *MNRAS*, 530, 1550, doi: [10.1093/mnras/stae933](https://doi.org/10.1093/mnras/stae933) 6,4

Íñiguez-Pascual, D., Torres, D. F., & Viganò, D. 2025, *MNRAS*, 541, 806, doi: [10.1093/mnras/staf1044](https://doi.org/10.1093/mnras/staf1044) 6,4

Icecube Collaboration, Abbasi, R., Ackermann, M., et al. 2023, *Science*, 380, 1338, doi: [10.1126/science.adc9818](https://doi.org/10.1126/science.adc9818) 6,3

Inc., W. R. 2024, *Mathematica*, Version 14.2, <https://www.wolfram.com/mathematica> 6,5

Jackson, J. D. 1998, *Classical electrodynamics* 3rd edition 2,1

Jones, F. C. 1965, *Physical Review*, 137, 1306, doi: [10.1103/PhysRev.137.B1306](https://doi.org/10.1103/PhysRev.137.B1306) 5

Kalapotharakos, C., Brambilla, G., Timokhin, A., Harding, A. K., & Kazanas, D. 2018, *ApJ*, 857, 44, doi: [10.3847/1538-4357/aab550](https://doi.org/10.3847/1538-4357/aab550) 1, 6.4

Kalapotharakos, C., & Contopoulos, I. 2009, *A&A*, 496, 495, doi: [10.1051/0004-6361:200810281](https://doi.org/10.1051/0004-6361:200810281) 1, 2.1

Kalapotharakos, C., Contopoulos, I., & Kazanas, D. 2012, *MNRAS*, 420, 2793, doi: [10.1111/j.1365-2966.2011.19884.x](https://doi.org/10.1111/j.1365-2966.2011.19884.x) 1

Kalapotharakos, C., Harding, A. K., & Kazanas, D. 2014, *ApJ*, 793, 97, doi: [10.1088/0004-637X/793/2/97](https://doi.org/10.1088/0004-637X/793/2/97) 1, 6.4

Kalapotharakos, C., Harding, A. K., Kazanas, D., & Brambilla, G. 2017, *ApJ*, 842, 80, doi: [10.3847/1538-4357/aa713a](https://doi.org/10.3847/1538-4357/aa713a) 1, 2.1, 3, 6.3, 6.4

Kalapotharakos, C., Harding, A. K., Kazanas, D., & Wadiasingh, Z. 2019, *ApJL*, 883, L4, doi: [10.3847/2041-8213/ab3e0a](https://doi.org/10.3847/2041-8213/ab3e0a) 1, 2.4, 6.4

Kalapotharakos, C., Wadiasingh, Z., Harding, A. K., & Kazanas, D. 2021, *ApJ*, 907, 63, doi: [10.3847/1538-4357/abcecc0](https://doi.org/10.3847/1538-4357/abcecc0) (a)

Kalapotharakos, C., Wadiasingh, Z., Harding, A. K., & Kazanas, D. 2022, *ApJ*, 934, 65, doi: [10.3847/1538-4357/ac78e3](https://doi.org/10.3847/1538-4357/ac78e3) 1, 1, 2.3, 3, 6, 4, 8, 6.3, 6.4

Kalapotharakos, C., Wadiasingh, Z., Harding, A. K., & Kazanas, D. 2023, *ApJ*, 954, 204, doi: [10.3847/1538-4357/ace972](https://doi.org/10.3847/1538-4357/ace972) 1, 1, 2.3, 2.4, 13, 5, 3, 5, 9, 5, 17, 6.4

Kerr, M. 2011, *ApJ*, 732, 38, doi: [10.1088/0004-637X/732/1/38](https://doi.org/10.1088/0004-637X/732/1/38) 6.3

Kerr, M., Wadiasingh, Z., Laviron, A., et al. 2025, *ApJ*(submitted) 4.1, 6.3, 6.5

Kirk, J. G., Skjæraasen, O., & Gallant, Y. A. 2002, *A&A*, 388, L29, doi: [10.1051/0004-6361:20020599](https://doi.org/10.1051/0004-6361:20020599) 1

Kuiper, L., & Hermsen, W. 2015, *MNRAS*, 449, 3827, doi: [10.1093/mnras/stv426](https://doi.org/10.1093/mnras/stv426) 6.2

List, F., Park, Y., Rodd, N. L., Schoen, E., & Wolf, F. 2025, arXiv e-prints, arXiv:2507.17804, doi: [10.48550/arXiv.2507.17804](https://doi.org/10.48550/arXiv.2507.17804) 6.3

Liu, K., Young, A., Wharton, R., et al. 2019, *ApJL*, 885, L10, doi: [10.3847/2041-8213/ab4da8](https://doi.org/10.3847/2041-8213/ab4da8) 5

Luo, J., Ransom, S., Demorest, P., et al. 2021, *ApJ*, 911, 45, doi: [10.3847/1538-4357/abe62f](https://doi.org/10.3847/1538-4357/abe62f) 6.3

Lyubarskii, Y. E. 1996, *A&A*, 311, 172 1, 6.2

Manchester, R. N., Hobbs, G. B., Teoh, A., & Hobbs, M. 2005, *AJ*, 129, 1993, doi: [10.1086/428488](https://doi.org/10.1086/428488) 1

Manconi, S., Calore, F., & Donato, F. 2024, *PhRvD*, 109, 123042, doi: [10.1103/PhysRevD.109.123042](https://doi.org/10.1103/PhysRevD.109.123042) 6.3

Mignani, R. P., Paladino, R., Rudak, B., et al. 2017, *ApJL*, 851, L10, doi: [10.3847/2041-8213/aa9c3e](https://doi.org/10.3847/2041-8213/aa9c3e) 5

Miller, M. C., Lamb, F. K., Dittmann, A. J., et al. 2019, *ApJL*, 887, L24, doi: [10.3847/2041-8213/ab50c5](https://doi.org/10.3847/2041-8213/ab50c5) (a)

Navas, S., et al. 2024, *Phys. Rev. D*, 110, 030001, doi: [10.1103/PhysRevD.110.030001](https://doi.org/10.1103/PhysRevD.110.030001) 6.3

Olausen, S. A., & Kaspi, V. M. 2014, *ApJS*, 212, 6, doi: [10.1088/0067-0049/212/1/6](https://doi.org/10.1088/0067-0049/212/1/6) 1

Olmschenk, G., Broadbent, E., Kalapotharakos, C., et al. 2025, *ApJ*, 991, 169, doi: [10.3847/1538-4357/ae03c0](https://doi.org/10.3847/1538-4357/ae03c0) (a)

Pétri, J. 2011, *MNRAS*, 412, 1870, doi: [10.1111/j.1365-2966.2010.18023.x](https://doi.org/10.1111/j.1365-2966.2010.18023.x) 1

Pétri, J. 2012, *MNRAS*, 424, 605, doi: [10.1111/j.1365-2966.2012.21238.x](https://doi.org/10.1111/j.1365-2966.2012.21238.x) 2.1

Pétri, J. 2022, *A&A*, 666, A5, doi: [10.1051/0004-6361/202243634](https://doi.org/10.1051/0004-6361/202243634) (b)

Philippov, A. A., & Spitkovsky, A. 2014, *ApJL*, 785, L33, doi: [10.1088/2041-8205/785/2/L33](https://doi.org/10.1088/2041-8205/785/2/L33) 1

Philippov, A. A., & Spitkovsky, A. 2018, *ApJ*, 855, 94, doi: [10.3847/1538-4357/aaabbc](https://doi.org/10.3847/1538-4357/aaabbc) 1, 6.4

Philippov, A. A., Spitkovsky, A., & Cerutti, B. 2015, *ApJL*, 801, L19, doi: [10.1088/2041-8205/801/1/L19](https://doi.org/10.1088/2041-8205/801/1/L19) 1

Ploeg, H., Gordon, C., Crocker, R., & Macias, O. 2020, *JCAP*, 2020, 035, doi: [10.1088/1475-7516/2020/12/035](https://doi.org/10.1088/1475-7516/2020/12/035) 6.3

Riley, T. E., Watts, A. L., Bogdanov, S., et al. 2019, *ApJL*, 887, L21, doi: [10.3847/2041-8213/ab481c](https://doi.org/10.3847/2041-8213/ab481c) (a)

Romani, R. W., & Watters, K. P. 2010, *ApJ*, 714, 810, doi: [10.1088/0004-637X/714/1/810](https://doi.org/10.1088/0004-637X/714/1/810) 4

Sautron, M., Pétri, J., Mitra, D., Dupuy-Junet, A., & Pietrin, M.-E. 2025, arXiv e-prints, arXiv:2510.15661, doi: [10.48550/arXiv.2510.15661](https://doi.org/10.48550/arXiv.2510.15661) 6.3

Shibanov, Y. A., Koptsevich, A. B., Sollerman, J., & Lundqvist, P. 2003, *A&A*, 406, 645, doi: [10.1051/0004-6361:20030652](https://doi.org/10.1051/0004-6361:20030652) 5

Shutt, T., Trbalic, B., Charles, E., et al. 2025, arXiv e-prints, arXiv:2502.14841, doi: [10.48550/arXiv.2502.14841](https://doi.org/10.48550/arXiv.2502.14841) 4.1

Skiathas, D., Kalapotharakos, C., Wadiasingh, Z., et al. 2025, *ApJ*, 994, 131, doi: [10.3847/1538-4357/adfbee](https://doi.org/10.3847/1538-4357/adfbee) 1

Smith, D. A., Bruel, P., Cognard, I., et al. 2019, *ApJ*, 871, 78, doi: [10.3847/1538-4357/aaf57d](https://doi.org/10.3847/1538-4357/aaf57d) 4.1

Smith, D. A., Abdollahi, S., Ajello, M., et al. 2023, *ApJ*, 958, 191, doi: [10.3847/1538-4357/acee67](https://doi.org/10.3847/1538-4357/acee67) 1, 2.3, 4, 6.2, (c)

Soudais, A., Cerutti, B., & Contopoulos, I. 2024, *A&A*, 690, A170, doi: [10.1051/0004-6361/202450238](https://doi.org/10.1051/0004-6361/202450238) (b)

Spitkovsky, A. 2006, *ApJL*, 648, L51, doi: [10.1086/507518](https://doi.org/10.1086/507518) 1, 2.1

Tabassum, S., & Lorimer, D. R. 2025, *ApJ*, 988, 78, doi: [10.3847/1538-4357/ade13f](https://doi.org/10.3847/1538-4357/ade13f) 6.3

Tchekhovskoy, A., Spitkovsky, A., & Li, J. G. 2013, MNRAS, 435, L1, doi: [10.1093/mnrasl/slt076](https://doi.org/10.1093/mnrasl/slt076) 2.1

Timokhin, A. N. 2006, MNRAS, 368, 1055, doi: [10.1111/j.1365-2966.2006.10192.x](https://doi.org/10.1111/j.1365-2966.2006.10192.x) 1

Timokhin, A. N., & Arons, J. 2013, MNRAS, 429, 20, doi: [10.1093/mnras/sts298](https://doi.org/10.1093/mnras/sts298) 6.4

Timokhin, A. N., & Harding, A. K. 2015, ApJ, 810, 144, doi: [10.1088/0004-637X/810/2/144](https://doi.org/10.1088/0004-637X/810/2/144) 6.2, 6.4

Timokhin, A. N., & Harding, A. K. 2019, ApJ, 871, 12, doi: [10.3847/1538-4357/aaf050](https://doi.org/10.3847/1538-4357/aaf050) 6.2, 6.4

Wadiasingh, Z., Baring, M. G., Gonthier, P. L., & Harding, A. K. 2018, ApJ, 854, 98, doi: [10.3847/1538-4357/aaa460](https://doi.org/10.3847/1538-4357/aaa460) 1

Wadiasingh, Z., Younes, G., Baring, M. G., et al. 2019, BAAS, 51, 292, doi: [10.48550/arXiv.1903.05648](https://doi.org/10.48550/arXiv.1903.05648) 1

Zdziarski, A. A., & Lightman, A. P. 1985, ApJL, 294, L79, doi: [10.1086/184513](https://doi.org/10.1086/184513) 6.2

Zyuzin, D., Shibanov, Y., Danilenko, A., Mennickent, R. E., & Zharikov, S. 2013, ApJ, 775, 101, doi: [10.1088/0004-637X/775/2/101](https://doi.org/10.1088/0004-637X/775/2/101) 5